Article

Cryptochrome–Timeless structure reveals circadian clock timing mechanisms

https://doi.org/10.1038/s41586-023-06009-4

Received: 26 July 2022

Accepted: 23 March 2023

Published online: 26 April 2023

Check for updates

Changfan Lin[1,2], Shi Feng[1,2], Cristina C. DeOliveira[1] & Brian R. Crane[1]✉

Circadian rhythms influence many behaviours and diseases[1,2]. They arise from oscillations in gene expression caused by repressor proteins that directly inhibit transcription of their own genes. The fly circadian clock offers a valuable model for studying these processes, wherein Timeless (Tim) plays a critical role in mediating nuclear entry of the transcriptional repressor Period (Per) and the photoreceptor Cryptochrome (Cry) entrains the clock by triggering Tim degradation in light[2,3]. Here, through cryogenic electron microscopy of the Cry–Tim complex, we show how a light-sensing cryptochrome recognizes its target. Cry engages a continuous core of amino-terminal Tim armadillo repeats, resembling how photolyases recognize damaged DNA, and binds a C-terminal Tim helix, reminiscent of the interactions between light-insensitive cryptochromes and their partners in mammals. The structure highlights how the Cry flavin cofactor undergoes conformational changes that couple to large-scale rearrangements at the molecular interface, and how a phosphorylated segment in Tim may impact clock period by regulating the binding of Importin-α and the nuclear import of Tim–Per[4,5]. Moreover, the structure reveals that the N terminus of Tim inserts into the restructured Cry pocket to replace the autoinhibitory C-terminal tail released by light, thereby providing a possible explanation for how the long–short Tim polymorphism adapts flies to different climates[6,7].

Circadian rhythms rely on cell-autonomous molecular clocks composed of transcriptional–translational feedback loops[1,2]. In the paradigm clock of *Drosophila melanogaster* (Fig. 1a), the transcriptional repressor proteins Per and Tim associate and accumulate in the cytosol before timed transport to the nucleus where they inhibit the transcription factors Clock (Clk) and Cycle (Cyc)[2,3] and thereby downregulate the expression of *per*, *tim* and other clock-controlled genes[2,3] (Fig. 1a). A cascade of Tim phosphorylation by the Shaggy (Sgg) and Ck2 kinases gates nuclear entry of Per–Tim to properly time the circadian oscillator[4]. Tim co-transports Per by binding directly to the nuclear import factor Importin-α1 (Impα1; ref. 5).

The fly clock is entrained by the flavoprotein Cry (Fig. 1a), which binds to Tim in the light (Fig. 1b) and directs it for proteasomal degradation[2,3,8]. CRY flavoproteins share a flavin-binding photolyase homology region (PHR) with the DNA repair enzyme photolyase but also contain a CRY C-terminal extension (CCE) that is specific for the function of a given CRY[9–11]. Cryptochromes from plants and type I cryptochromes from animals sense light to reset the circadian clock; type II cryptochromes from animals repress transcription in a light-independent manner by binding the PER proteins and directly inhibiting CLK[9,10]. In *Drosophila*, photoreduction of the Cry FAD to the anionic semiquinone by a tryptophan tetrad (W342, W397, W420 and W394) triggers release of a C-terminal tail (CTT) helix[12–18] (Fig. 1b). Photoreduced Cry resets Tim levels by binding Tim and recruiting the E3 ubiquitin ligase Jetlag (Jet)[8,19,20] (Fig. 1a). Recognition of Tim by Cry is hence the molecular event that sensitizes the clock to light. Although light-sensing CRY flavoproteins have also been developed as powerful tools for optogenetic applications[21,22]; there is little direct structural information on how light-activated cryptochromes recognize their targets.

Cry–Tim structure determination

To overcome the challenge of isolating sufficient amounts of Tim (1,398 residues) for structural characterization by cryogenic electron microscopy (cryo-EM), we developed an insect (*Drosophila* S2)-cell-based expression and nanobody-based affinity purification workflow for isolation of the 264-kDa Cry–Tim complex (Supplementary Methods Overview). To produce Cry–Tim, a CryΔ variant that lacks the 22-residue CCE[23] and therefore binds Tim constitutively[24,25] was co-transfected and expressed in S2 cells with the Tim short isoform *S*-Tim. Coexpression with CryΔ substantially increased Tim levels (see Methods). Nanobody-based affinity resin directed at a 13-residue ALFA tag allowed enrichment and elution of the complex. Complex homogeneity was further improved, and aggregation was avoided by crosslinking with the lysine-specific reagent disuccinimidyl sulfoxide (DSSO) followed by separation by size-exclusion chromatography (Extended Data Fig. 1). Eluted samples were applied directly to glow-discharged Quantifoil grids, vitrified and imaged on a 200-keV Talos Arctica microscope equipped with a Gatan Quantum LS energy filter and a K3 direct electron camera. Two out of three 3-dimensional classes were refined to yield global 3.48-Å (about 98,000 particles)

[1]Department of Chemistry and Chemical Biology, Cornell University, Ithaca, NY, USA. [2]These authors contributed equally: Changfan Lin, Shi Feng. ✉e-mail: bc69@cornell.edu

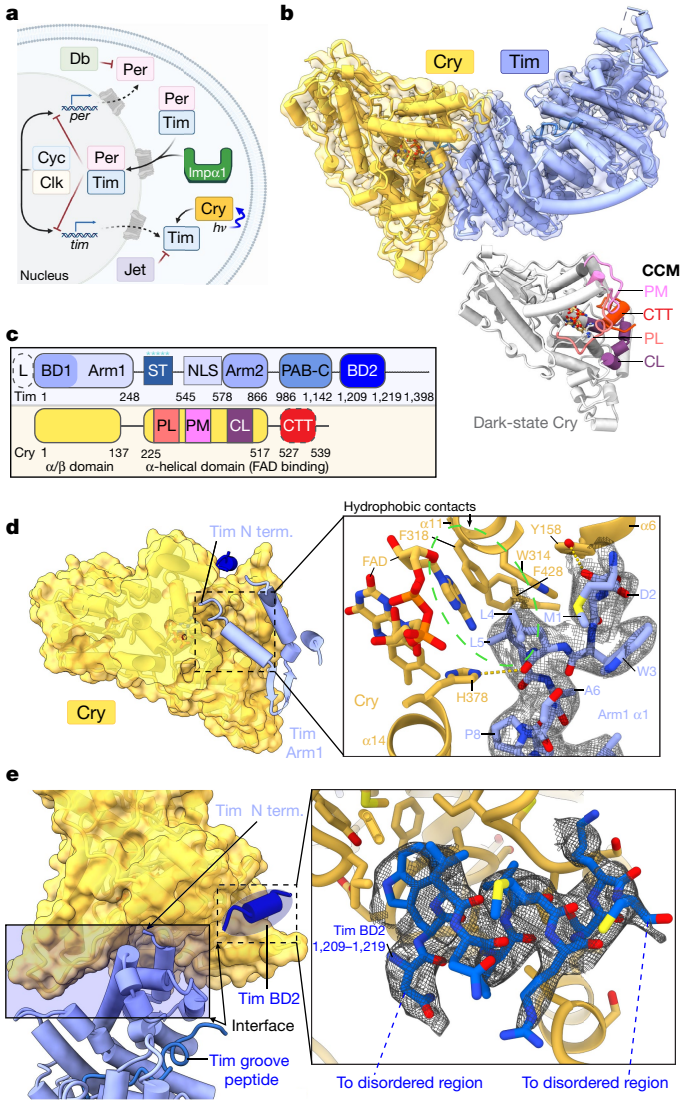

Fig. 1 | Cryo-EM structure of the Cry–Tim complex. a, *Drosophila* Cry entrains the circadian clock by initiating degradation of Tim in light. Jet, Per, Doubletime (Db), Cyc, Clk and Impα1 compose the core circadian oscillator. *hν* represents photon energy, in which *h* is the Planck constant and *ν* is the photon frequency. **b**, Cry–Tim docked into the electron density map. Dark-state Cry shown at the bottom (grey; Protein Data Bank (PDB) ID: 4GU5). **c**, Domain arrangements and key regions of Cry and Tim. Features of Tim: Cry-binding domains (Cry BD1, 1–234; Cry BD2, 1,133–1,398 containing recognition helix 1,209–1,219), serine/threonine-rich region (ST, 270–290) with key phosphorylation sites marked with asterisks (S274, T278, T282, S286 and S290), ARM1 (1–248), ARM2 (578–866), nuclear localization sequence (NLS, 545–578), Parp1-binding domain (PAB, 986–1,142; Tim-C, 1,051–1,096), 23-residue *L*-Tim extension (L; 23 amino acids). Features of Cry: phosphate-binding loop (PL, 249–263), protrusion motif (PM, 288–306), C-terminal lid (CL, 420–446), CTT (519–542, absent in CryΔ). **d**, N terminus of Tim inserts into the primary flavin-binding pocket. Shown is 2.4-Å-resolution local electron density with notable hydrogen bonds (yellow dashes) and hydrophobic contacts (green dashed oval). **e**, Interface between Cry and Tim (blue shaded area), Tim groove peptide (in navy blue) and peripheral helix (fitted with 1,209–1,219 provisionally, blue). Inset shows the interactions between Tim 1,209–1,219 and Cry superimposed with electron density. Schematic in **a** created with BioRender.com.

and 3.3-Å (about 160,000 particles) maps of the complex (Extended Data Fig. 1 and Supplementary Table 1). We built an atomic model based on better resolved Tim density in the 3.3 Å map (Supplementary Video 1). Local resolution at the complex interface and within the body exceeds 2.5 Å.

Cry recognizes the Tim N terminus

The core of Tim revealed in the Cry–Tim complex (residues 1–248, 545–866 and 986–1,142; Fig. 1b, Extended Data Fig. 2 and Supplementary Video 1) forms a continuous right-handed supercoil of armadillo (ARM) three-helix repeats[26] in which two ARM domains discontinuous in sequence (ARM1 and ARM2; Fig. 1c) associate by swapping their terminal helices (Extended Data Fig. 2). Tim resembles mammalian TIM (mTIM, see below)[27] but contains an N-terminal extension that binds to Cry (Fig. 1d). The Cry PHR comprises an N-terminal α/β domain and a C-terminal helical domain that harbours the FAD isoalloxazine ring in a central four-helix bundle formed by α13–α16 (Fig. 1b,c, Extended Data Fig. 3 and Supplementary Video 1; refs. 28–30). N-terminal to the bundle, helices α8–α11 compose the top of the flavin-binding pocket and interact with the FAD phosphate groups and adenosine moiety (Extended Data Fig. 3). In this cofactor-capping region, the phosphate-binding loop (residues 249–263) following α8 and the protrusion motif (residues 288–306) following α10 distinguish cryptochromes from photolyases[28] (Fig. 1c). The phosphate-binding loop, the protrusion motif and the serine-rich C-terminal lid (residues 420–446) together compose the C-terminal coupled motif (CCM; Fig. 1c and Extended Data Fig. 3) that changes sensitivity to proteolysis when Cry becomes light activated[13].

Tim forms a discontinuous interface with Cry both at the N terminus and C terminus (Fig. 1b–e). The principal Cry–Tim interface buries about 1,862 Å^2 (49 residues) and 1,807 Å^2 (52 residues) of solvent-accessible surface area on Tim and Cry, respectively. Tim primarily binds to Cry through the first three helices of the N-terminal Arm domain (Fig. 1d,e). Arm1 α1 binds across Cry α17 and inserts directly into the flavin-binding pocket replacing the Cry CTT (Figs. 1d and 2a and Extended Data Fig. 4a). The contact is dominated by Tim ARM1 α1–α3, ARM1 α7 and the ARM1 α9–α10 loop that mesh against the Cry CCM (Fig. 1e and Extended Data Figs. 2 and 4). At the centre of the interface, Met1 and Asp2 extend out from α1 with Met1 packing against the Trp3 indole and embedding among several elements: Tyr250 and Leu251 of the Cry phosphate-binding loop, Gly310 on α11 and Tyr158-Gln159 on the α5–α6 loop that extends down from the Cry α/β domain (Extended Data Figs. 3 and 5). Tim Leu4 and Leu5 insert deep into the pocket adjacent to Cry Trp314 and the FAD adenine moiety (Fig. 1d). Tim ARM1 α2 contacts the Cry C-terminal lid and ARM1 α7 contacts the Cry protrusion motif, wherein the α10 helix lengthens to project the tip region towards the methionine-rich Arm1 α9–α10 loop at the interface periphery (Extended Data Figs. 4c,d).

Cry–Tim implications for photoadaptation

The recognition of ARM1 α1 of Tim by Cry (Fig. 1d) may explain an evolutionary adaptation in light-sensing by flies. A *D. melanogaster tim* allele (*ls-tim*) causes differential expression of two isoforms; *S*-Tim, which begins at the N-terminal methionine residue found in the structure, and *L*-Tim, which extends by an additional 23 N-terminal residues owing to introduction of an alternative translational start site[6,7] (Fig. 1b). The frequency of *ls-tim* correlates with geographical latitude and may confer a beneficial preference for more robust rhythms and a diapause state of dormancy in climates of more variable light and cooler temperatures. *L*-Tim reduces interaction with Cry by yeast two-hybrid screening, has greater stability in fly heads and diminishes clock responses to light[20,31]. The N terminus of Met1 projects into a solvent channel at the interface of the two proteins that could therefore accommodate the *L*-Tim extension (Fig. 1d and Extended Data Fig. 6a). However, the recognition of *S*-Tim by Cry at the N terminus will be altered by the *L*-Tim extension (Fig. 1d), thereby potentially explaining the capacity of *ls-tim* to alter the light sensitivity of flies.

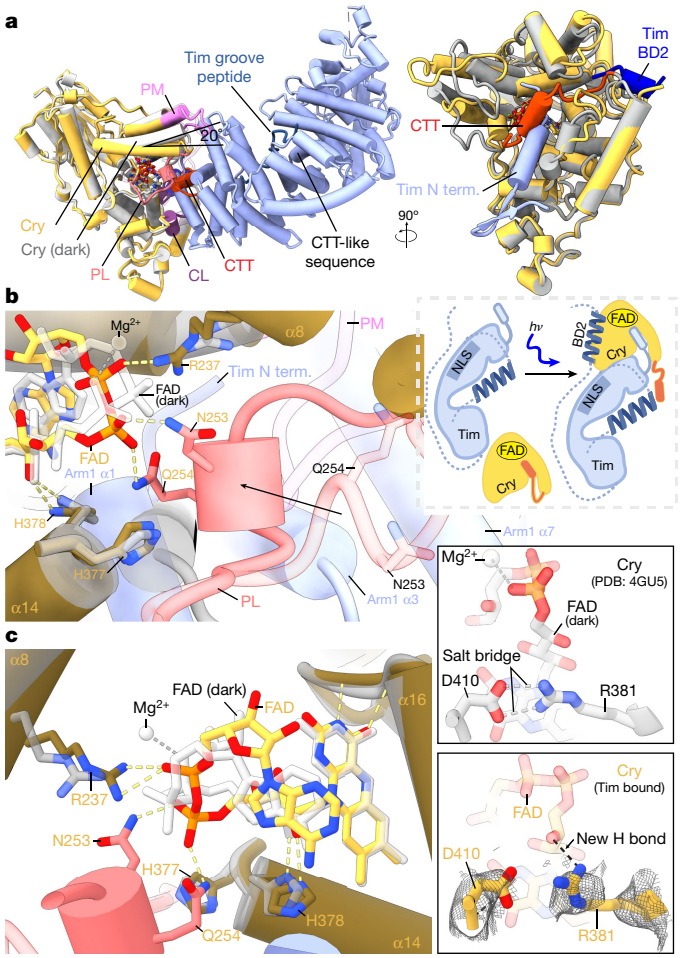

Fig. 2 | Conformational changes of FAD and the Cry CCM after binding Tim. **a**, Cry–Tim (Cry, yellow; Tim, blue) in superposition with dark-state Cry (grey) shown from the side (left) and at a 90° rotation (right) that shows only the Tim N terminus (term.) and peripheral binding domain 2 (BD2). The N terminus of Tim (right) replaces the Cry CTT (red), as depicted in the dashed-outline inset schematic directly below. Structural elements designated as in Fig. 1. A CTT-like sequence on Tim (617–626) that in isolation binds light-state Cry[13] locates in the Arm core remote from the interface and is thus unlikely to be a binding determinant. **b**, The phosphate-binding loop (dark pink) collapses into the flavin pocket (long black arrow) and N253 and E254 hydrogen bond (yellow dashes) with the FAD diphosphate conformation (red, orange) that differs substantially from that of the dark state (white bonds). **c**, The diphosphate group rearranges, R237 replaces the Mg^{2+} counter ion and H377 anchors the new position of the loop. The D410–R381 salt bridge in the dark state (top right inset) appears to break in response to the new conformation of the ribose backbone (bottom box). Reduced side-chain density of R381 suggests increased flexibility in the Tim complex (bottom right inset). Schematic of **a** in inset created with BioRender.com.

A discontinuous Tim-binding element

In addition to the principal interaction between Tim ARM1 and Cry, strong electron density for a Tim helical segment is evident among the C-terminal lid, the C-terminal end of the last Cry PHR helix (α20) and the α5–α6 loop that projects down from the α/β domain (Fig. 1e and Extended Data Fig. 3). This Tim helix buries 496 $Å^2$ of surface area, interacts with the light-state configuration of the C-terminal lid and binds at the position occupied by the residues that link α20 to the CTT in the dark-state structure, thereby supporting results from interaction studies[25] and providing further evidence that the CTT undocks from the flavin pocket after light activation[13,15,17]. There are no connections of this density to the ordered Tim ARM core, and thus its sequence assignment is provisional. Nevertheless, after computational modelling of many predicted helical sequence registers, several gave reasonable agreement with the density and stereochemical constraints of the site; however, of these segments, only 1,209–1,219 was also predicted to occupy the site by Alphafold2.1 (Extended Data Fig. 7a; ref. 32). To further validate binding by the C-terminal disordered region, we carried out a SWFTI (select western blot–free tagged protein interaction) assay (Extended Data Fig. 8) with Tim truncations and the Cry variant H377L that exhibits constitutive binding to Tim but also retains the CTT[16]. Cry bound to Tim 1–1,132 and to Tim 571–1,398 similarly, but with reduced affinity compared to that of full-length *S*-Tim. Tim 1,133–1,398 (binding domain 2), which contains the proposed peripheral helix, alone bound to Cry(H377L) (Extended Data Fig. 8). A known alteration of human TIM that removes the analogous region (R1081X) causes familial advanced sleep phase by reducing interactions between mTIM and mCRY2 (ref. 33). Thus, although the roles of mCRY and Cry are not the same in animals and insects[2], they may produce similar interactions with the otherwise disordered C termini of their respective TIM proteins. These interactions may include competition with Per because Tim 1,209–1,219 associates with Cry in a region that coincides with where mCRY binds the mPER proteins[34–36] (Extended Data Fig. 9a).

TIM proteins diverge in function

Tim and mTIM have similar structures in their respective ordered regions (Extended Data Fig. 9b), but their functions diverge. In fact, mTIM is more closely related to the *Drosophila* Timeout protein (Tim2) than to Tim itself[27,33]. Although mTIM and Tim2 play some role in circadian rhythms, neither are central constituents of the core mammalian oscillator[2]. By contrast, mTIM and its homologues (Tof1 and Swi1 in yeast, and tim-1 in *Caenorhabditis elegans*) stabilize replication forks during DNA replication, pair sister chromatids and regulate S-phase checkpoints[37]. Tof1 participates in the large replisome complex in which it binds directly to double-stranded DNA[38] (Extended Data Fig. 9d). Tim and mTIM share a C-terminal domain (PAB) that includes a conserved stretch of the Tim C region (residues 1,051–1,096; 'TIM C_domain' in ref. 33) and binds poly-(ADP-ribose) polymerase 1 (PARP1) in mTIM[39]. However, just as the N terminus of mTIM is unsuited to bind mCRY, the Tim PAB is unlikely to bind to Parp1 because it differs in the interface elements displayed by mTIM (Extended Data Fig. 9c). Thus, details of the respective structures indicate that the roles of fly Tim for the stabilization and co-transport of Per are probably distinct from those of mTIM, Tof1 and Tim2 for genome maintenance.

Flavin conformational changes

Pronounced changes in the Cry cofactor-binding pocket (Fig. 2a) after binding of Tim involve repositioning of the adenosine and ribose moieties, a large switch in the conformation of the diphosphate groups and refolding of the C-terminal lid to interact with Tim ARM1 α1 and α2. Moreover, the phosphate-binding loop collapses into the flavin pocket to allow Asn253, Gln254 and Gln311 to hydrogen bond with the FAD phosphates (Extended Data Fig. 5a). Tyr250 and Leu251 interact with the FAD pocket and make space for the top of Tim ARM1 α3 to insert Phe58 behind the new conformation of the phosphate-binding loop (Fig. 2b and Extended Data Fig. 5a). In addition, cofactor-capping helix α8 tilts 20° towards the FAD diphosphates as Arg237 replaces the FAD Mg^{2+} counter ion, for which no electron density is observed (Fig. 2c and Extended Data Fig. 5b). The FAD adenine ring slides 1.5 Å relative to the unbound structure, an adjustment compensated by a shift of Phe318 and harbouring helix α11 (Extended Data Fig. 5b). The 262-to-264 loop also changes structure to accommodate the new diphosphate conformation and Gln311 swivels away from Tim Leu4 (Extended Data Fig. 5a,c). The primary light-sensitive reaction of flavin photoreduction

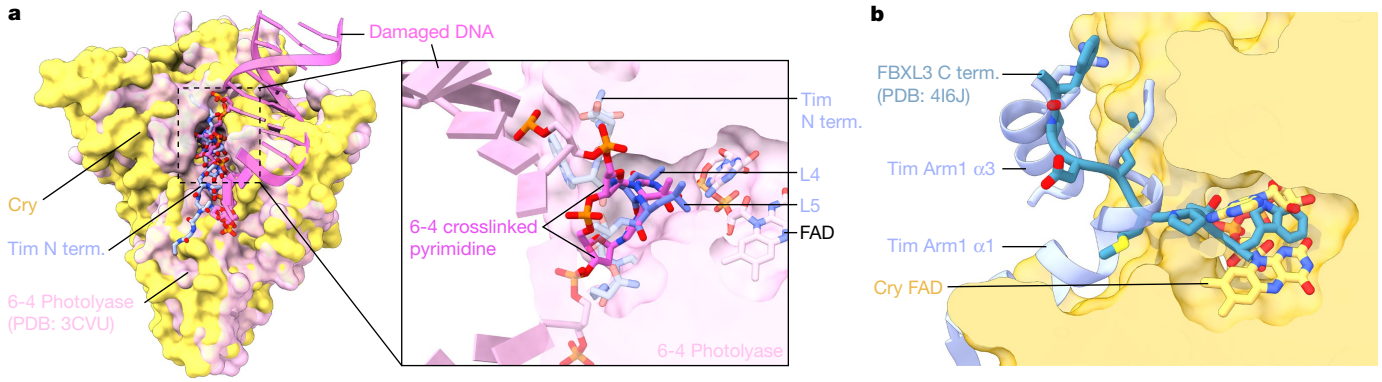

Fig. 3 | Conservation of recognition modes by CRY family members. **a**, The interaction of Cry with Tim corresponds closely to how 6-4 photolyase recognizes the 6-4 pyrimidine lesion in damaged DNA (PDB ID: 3CVU). Tim L4 and L5 superimpose on the crosslinked bases and the Tim ARM1 α1 polypeptide closely follows the path of 5′-to-3′ strand-separated DNA. **b**, The Tim and FAD contacts of Cry mimic the interaction of apo-mCRY with the C terminus of the FBXL3 E3 ligase (PDB ID: 4I6J).

and CTT release precedes Tim binding; however, these events may induce conformational changes of the FAD and serve to restructure Cry for downstream target engagement.

The Cry–Tim complex was purified under light. Although the cofactor redox state could not be verified on the cryo-EM grids, Cry light sensitivity studies[15] indicate that the Cry flavin should be photochemically reduced under these conditions. Regardless, Tim probably stabilizes features of the light-state structure. In support of light-activated Cry in the complex, an Asp410-to-Arg381 salt bridge critical for flavin binding and the site of the light-insensitive *cryb* mutation[40] appears to break in response to the new conformation of the ribose backbone (Fig. 2c), in keeping with predictions of light activation from molecular dynamics simulations[41]. Two conserved histidine residues within the flavin pocket, His377 and His378, participate in the PL catalytic mechanism and are implicated in CTT release and Tim binding[16,18,42]. In the unbound state, His378 ND1 hydrogen bonds with O2′ of the FAD ribose, but in the Tim complex, His378 tilts away from the ribose hydroxyl to hydrogen bond to the Tim Leu5 carbonyl with NE2 (Fig. 2b,c and Extended Data Fig. 5b). Substitutions at His378 still allow CTT release, but on/off switching is less robust[16,42]. Protonation of His378 NE2 is probably required for it to interact with the Tim Leu5 carbonyl and His378 protonation may be responsive to the flavin redox state. The H377L substitution substantially increases the binding affinity to Tim in both light and dark[16]. Unexpectedly, His377 does not contact Tim directly but rather anchors the restructured phosphate-binding loop by hydrogen bonding to the Asn253 carbonyl (Fig. 2c). Cry flavin reoxidation is reversible, as is redocking of the CTT[13,15,17], which would complete with Tim for the flavin pocket and hence promote Cry release. However, clock resetting does not require complex dissociation because both Tim and Cry are degraded by the ubiquitin–proteosome pathway after their association[8,20].

Relationships of cryptochromes and photolyases

The interaction of Cry with Tim corresponds closely to how 6-4 photolyase recognizes the 6-4 crosslinked pyrimidine lesion in damaged DNA (Fig. 3a). Indeed, Tim α1 residues Leu4 and Leu5 superimpose with the crosslinked base and the Tim polypeptide closely follows the path of 5′-to-3′ strand-separated DNA[43] (Fig. 3a). Key residues in the pocket also share identity and similar positions, with the notable exception of photolyase Tyr306, which as a phenylalanine in Cry contacts the Leu5 side chain. Tim and FAD also combine in Cry to mimic interactions of the FBXL3 E3 ligase with apo-mCRY for their ubiquitin-mediated degradation[44] (Fig. 3b). E3 ligase recruitment to Cry could be similar only if the flavin is released, which does not occur on Cry–Tim association. More likely, the E3 ligases recognize structural features unique to the complex. Despite similarities at the primary cofactor pocket, the phosphate-binding loop, protrusion motif and C-terminal lid differ in both sequence and conformation among photolyase, mCRY and Cry. Cry also contains a secondary pocket between its two domains that in photolyase binds antenna cofactors and in mCRY mediates contacts with other clock components[9,45]. No cofactors or other constituents are found within the secondary pocket of the Cry–Tim structure; however, it composes a deep cleft typical of a recognition motif (Extended Data Fig. 6b).

Regulation of Tim nuclear entry

The Tim structure provides insight into the gating of Tim–Per nuclear entry by the interaction between Tim and Impα1. Tim is homologous to the β-catenins, their related family members (hmp-2, p120, plakoglobin, plakophilin and sys-1) and the importin-α/β karyopherins involved in nuclear transport[5,26,46]. These Arm proteins conserve a positively charged groove on the concave side of their super-helical crescents where they bind extended peptide chains, such as nuclear localization signals[47,48] (Fig. 4a,b and Extended Data Fig. 10). Two substitutions known to block nuclear entry by reducing interactions between Tim and Impα1 (Thr90Ala and Pro92Leu; *S*-Tim numbering)[5] localize within the Tim groove (Fig. 4b) but do not interact with the Tim nuclear localization sequence, which rather extends in a helix along the convex side of the protein (Fig. 4c). An extended polypeptide with α-helical character binds into the Tim groove adjacent to catenin-conserved arginine (84,165) and asparagine (88,166) residues (Extended Data Fig. 10) and Thr90 and Pro92 (Fig. 4b). Crosslinking mass spectrometry revealed that Tim Lys313 and Lys328 in the disordered Tim domain (249–545) react with lysine residues in the groove and towards the bottom of the crescent (Fig. 4c and Extended Data Fig. 10), whereas lysine residues in other disordered regions (400–544; 784–991; 1,129–1,398) show little crosslinking to Tim or Cry. After extensive modelling, the sequence Ser283–Thr303 was provisionally assigned as the most reasonable fit to the polypeptide density (Extended Data Fig. 7b). This assignment places Asp287 and Asn291 adjacent to the conserved asparagine and arginine residues and occludes the Thr90 and Pro92 residues involved in Impα1 binding (Fig. 4b).

Phosphorylation of the Tim ST stretch of Sgg and Ck2 target sites (Sgg: Ser274, Thr278; Ck2: Thr282, Ser286, Ser290; Figs. 1b and 4b) increases nuclear entry rates of Tim in pacemaker cells known as small lateral ventral neurons[4]. The Ser283–Thr303 polypeptide bound within the Tim groove contains Ser286 and Ser290, which belong to this region of regulatory sites[4]. Thus, the structure suggests that phosphorylation at these sites displaces Tim ST from the groove to expose

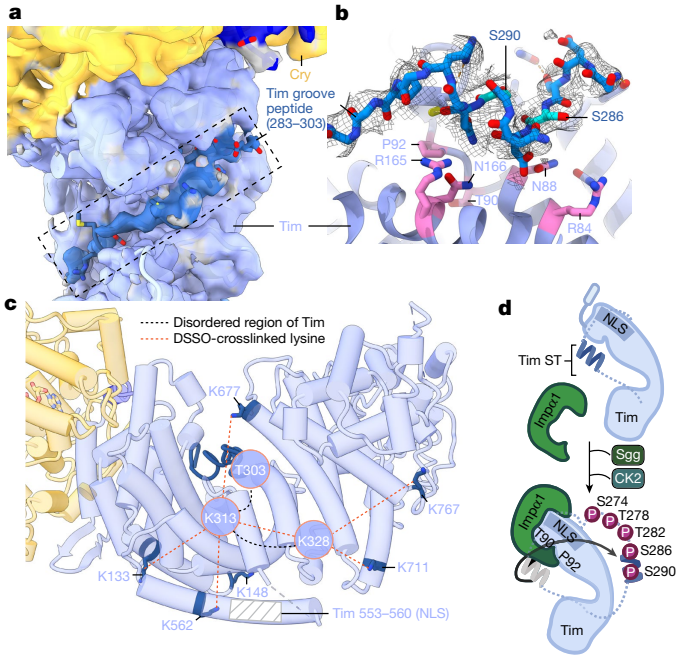

Fig. 4 | A structural basis for regulation of TIM nuclear entry. a, Electron density (dark blue) for an extended polypeptide resides within a groove wherein members of the β-catenin and α-importin proteins bind their target sequences. **b**, The Tim groove peptide density shown with the sequence assignment S283–T303. The peptide interacts with β-catenin-conserved asparagine and arginine residues and buries residues important for Impα1 binding (T90 and P92). **c**, DSSO-mediated lysine crosslinking patterns of disordered residues K313 and K328 shown on the Tim structure. K313 and K328 produce a pattern of crosslinking that localizes them to a position consistent with placement of the S283–T303 groove peptide. The Tim NLS lies in a helix adjacent to the groove but does not occlude T90 and P92. **d**, Schematic of proposed nuclear entry mechanism of Tim. Phosphorylation of the Tim ST region by Sgg and Ck2 releases the ST region from the Tim groove to expose Tim T90 and P92. Impα1 binds Tim adjacent to T90 and P92, while also binding the Tim NLS within a structurally analogous ARM groove of its own. Schematic in **d** created with BioRender.com.

the Thr90–Pro92 recognition motif for Impα1 and thereby initiate nuclear import (Fig. 4d). Thus, key delays that tune the clock period through nuclear entry probably depend on the interactions of a Tim autoinhibitory segment that alter following its timed phosphorylation by circadian kinases.

The Cry–Tim structure reveals how a light-sensing cryptochrome engages its target. It also provides insight into how evolutionary relationships among the component proteins compose regulatory circuits. Swapping the auxiliary CTT of Cry for the variable N terminus of Tim not only sets the circadian oscillator but also tunes its light sensitivity. In this interaction, the ability of Tim to serve as a peptide mimetic for a PL DNA substrate underscores how conserved structural features of photolyases are also utilized by cryptochromes. In gating its partnership with Cry, Tim shares an autoinhibitory mechanism that resembles that which regulates Importin-α[48–50]. The striking changes in FAD geometry that couple to Cry conformational rearrangement and Tim binding were unexpected. These new insights raise questions as to whether other flavoprotein light sensors share similar mechanisms to convey light or redox signals from their cofactors.

Online content

Any methods, additional references, Nature Portfolio reporting summaries, source data, extended data, supplementary information, acknowledgements, peer review information; details of author contributions and competing interests; and statements of data and code availability are available at https://doi.org/10.1038/s41586-023-06009-4.

1. Takahashi, J. S. Transcriptional architecture of the mammalian circadian clock. *Nat. Rev. Genet.* **18**, 164–179 (2017).
2. Crane, B. R. & Young, M. W. Interactive features of proteins composing eukaryotic circadian clocks. *Ann. Rev. Biochem.* **83**, 191–219 (2014).
3. Foley, L. E. & Emery, P. *Drosophila* cryptochrome: variations in blue. *J. Biol. Rhythms* **35**, 16–27 (2020).
4. Top, D., Harms, E., Syed, S., Adams, E. L. & Saez, L. GSK-3 and CK2 kinases converge on Timeless to regulate the master clock. *Cell Rep.* **16**, 357–367 (2016).
5. Jang, A. R., Moravcevic, K., Saez, L., Young, M. W. & Sehgal, A. *Drosophila* TIM binds Importin α1, and acts as an adapter to transport PER to the nucleus. *PLOS Genet.* **11** e004974 (2015).
6. Tauber, E. et al. Natural selection favors a newly derived timeless allele in *Drosophila melanogaster*. *Science* **316**, 1895–1898 (2007).
7. Deppisch, P. et al. Adaptation of *Drosophila melanogaster* to long photoperiods of high-latitude summers is facilitated by the *ls-timeless* allele. *J. Biol. Rhythms* **37**, 185–201 (2022).
8. Lin, F. J., Song, W., Meyer-Bernstein, E., Naidoo, N. & Sehgal, A. Photic signaling by cryptochrome in the *Drosophila* circadian system. *Mol. Cell. Biol.* **21**, 7287–7294 (2001).
9. Chaves, I. et al. The cryptochromes: blue light photoreceptors in plants and animals. *Annu. Rev. Plant Biol.* **62**, 335–364 (2011).
10. Ozturk, N. Phylogenetic and functional classification of the photolyase/cryptochrome family. *Photochem. Photobiol.* **93**, 104–111 (2017).
11. Parico, G. C. G. et al. The human CRY1 tail controls circadian timing by regulating its association with CLOCK:BMAL1. *Proc. Natl Acad. Sci. USA* **117**, 27971–27979 (2020).
12. Berndt, A. et al. A novel photoreaction mechanism for the circadian blue light photoreceptor *Drosophila* cryptochrome. *J. Biol. Chem.* **282**, 13011–13021 (2007).
13. Vaidya, A. T. et al. Flavin reduction activates *Drosophila* cryptochrome. *Proc. Natl Acad. Sci. USA* **110**, 20455–20460 (2013).
14. Ozturk, N., Selby, C. P., Annayev, Y., Zhong, D. & Sancar, A. Reaction mechanism of *Drosophila* cryptochrome. *Proc. Natl Acad. Sci. USA* **108**, 516–521 (2011).
15. Lin, C. F., Top, D., Manahan, C. C., Young, M. W. & Crane, B. R. Circadian clock activity of cryptochrome relies on tryptophan-mediated photoreduction. *Proc. Natl Acad. Sci. USA* **115**, 3822–3827 (2018).
16. Lin, C., Schneps, C. M., Chandrasekaran, S., Ganguly, A. & Crane, B. R. Mechanistic insight into light-dependent recognition of Timeless by *Drosophila* Cryptochrome. *Structure* **30**, 851–861 (2022).
17. Chandrasekaran, S. et al. Tuning flavin environment to detect and control light-induced conformational switching in *Drosophila* cryptochrome. *Commun. Biol.* **4**, 249 (2021).
18. Ganguly, A. et al. Changes in active site histidine hydrogen bonding trigger cryptochrome activation. *Proc. Natl Acad. Sci. USA* **113**, 10073–10078 (2016).
19. Koh, K., Zheng, X. Z. & Sehgal, A. JETLAG resets the *Drosophila* circadian clock by promoting light-induced degradation of TIMELESS. *Science* **312**, 1809–1812 (2006).
20. Peschel, N., Chen, K. F., Szabo, G. & Stanewsky, R. Light-dependent interactions between the *Drosophila* circadian clock factors Cryptochrome, Jetlag, and Timeless. *Curr. Biol.* **19**, 241–247 (2009).
21. Yu, D. et al. Optogenetic activation of intracellular antibodies for direct modulation of endogenous proteins. *Nat. Methods* **16**, 1095–1100 (2019).
22. Gil, A. A. et al. Optogenetic control of protein binding using light-switchable nanobodies. *Nat. Commun.* **11**, 4044 (2020).
23. Busza, A., Emery-Le, M., Rosbash, M. & Emery, P. Roles of the two *Drosophila* CRYPTOCHROME structural domains in circadian photoreception. *Science* **304**, 1503–1506 (2004).
24. Dissel, S. et al. A constitutively active cryptochrome in *Drosophila melanogaster*. *Nat. Neurosci.* **7**, 834–840 (2004).
25. Hemsley, M. J. et al. Linear motifs in the C-terminus of *D-melanogaster* cryptochrome. *Biochem. Biophys. Res. Commun.* **355**, 531–537 (2007).
26. Vodovar, N., Clayton, J. D., Costa, R., Odell, M. & Kyriacou, C. P. The *Drosophila* clock protein Timeless is a member of the Arm/HEAT family. *Curr. Biol.* **12**, R610–R611 (2002).
27. Holzer, S. et al. Crystal structure of the N-terminal domain of human Timeless and its interaction with Tipin. *Nucleic Acids Res.* **45**, 5555–5563 (2017).
28. Zoltowski, B. D. et al. Structure of full-length *Drosophila* cryptochrome. *Nature* **480**, 396–399 (2011).
29. Levy, C. et al. Updated structure of *Drosophila* cryptochrome. *Nature* **495**, E3–E4 (2013).
30. Czarna, A. et al. Structures of *Drosophila* cryptochrome and mouse cryptochrome1 provide insight into circadian function. *Cell* **153**, 1394–1405 (2013).
31. Sandrelli, F. et al. A molecular basis for natural selection at the timeless locus in *Drosophila melanogaster*. *Science* **316**, 1898–1900 (2007).
32. Jumper, J. et al. Highly accurate protein structure prediction with AlphaFold. *Nature* **596**, 583–589 (2021).
33. Kurien, P. et al. TIMELESS mutation alters phase responsiveness and causes advanced sleep phase. *Proc. Natl Acad. Sci. USA* **116**, 12045–12053 (2019).
34. Schmalen, I. et al. Interaction of circadian clock proteins CRY1 and PER2 is modulated by zinc binding and disulfide bond formation. *Cell* **157**, 1203–1215 (2014).
35. Fribourgh, J. L. et al. Dynamics at the serine loop underlie differential affinity of cryptochromes for CLOCK:BMAL1 to control circadian timing. *Elife* **9**, e55275 (2020).
36. Nangle, S. N. et al. Molecular assembly of the Period-Cryptochrome circadian transcriptional repressor complex. *Elife* **3**, e03674 (2014).
37. Engelen, E. et al. Mammalian TIMELESS is involved in period determination and DNA damage-dependent phase advancing of the circadian clock. *PLoS ONE* **8**, e56623 (2013).
38. Baretic, D. et al. Cryo-EM structure of the fork protection complex bound to CMG at a replication fork. *Mol. Cell* **78**, 926–940 (2020).

39. Xie, S. et al. Timeless interacts with PARP-1 to promote homologous recombination repair. *Mol. Cell* **60**, 163–176 (2015).
40. Stanewsky, R. et al. The cry(b) mutation identifies cryptochrome as a circadian photoreceptor in *Drosophila*. *Cell* **95**, 681–692 (1998).
41. Wang, Y. J., Veglia, G., Zhong, D. P. & Gao, J. L. Activation mechanism of *Drosophila* cryptochrome through an allosteric switch. *Sci. Adv.* **7**, eabg3815 (2021).
42. Berntsson, O. et al. Photoactivation of *Drosophila melanogaster* cryptochrome through sequential conformational transitions. *Sci. Adv.* **5**, eaaw1531 (2019).
43. Glas, A. F., Schneider, S., Maul, M. J., Hennecke, U. & Carell, T. Crystal structure of the T(6-4)C lesion in complex with a (6-4) DNA photolyase and repair of UV-induced (6-4) and Dewar photolesions. *Chemistry* **15**, 10387–10396 (2009).
44. Nangle, S., Xing, W. M. & Zheng, N. Crystal structure of mammalian cryptochrome in complex with a small molecule competitor of its ubiquitin ligase. *Cell Res.* **23**, 1417–1419 (2013).
45. Rosensweig, C. et al. An evolutionary hotspot defines functional differences between CRYPTOCHROMES. *Nat. Commun.* **9**, 1138 (2018).
46. Tewari, R., Bailes, E., Bunting, K. A. & Coates, J. C. Armadillo-repeat protein functions: questions for little creatures. *Trends Cell Biol.* **20**, 470–481 (2010).
47. Choi, H. J. et al. A conserved phosphorylation switch controls the interaction between cadherin and β-catenin in vitro and in vivo. *Dev. Cell* **33**, 82–93 (2015).
48. Goldfarb, D. S., Corbett, A. H., Mason, D. A., Harreman, M. T. & Adam, S. A. Importin α: a multipurpose nuclear-transport receptor. *Trends Cell Biol.* **14**, 505–514 (2004).
49. Catimel, B. et al. Biophysical characterization of interactions involving importin-α during nuclear import. *J. Biol. Chem.* **276**, 34189–34198 (2001).
50. Harreman, M. T., Hodel, M. R., Fanara, P., Hodel, A. E. & Corbett, A. H. The auto-inhibitory function of importin α is essential in vivo. *J. Biol. Chem.* **278**, 5854–5863 (2003).

Methods

Cloning

All DNA constructs (Supplementary Information) were built by a modified Gibson assembly method and Q5 polymerase-based mutagenesis with home-made reaction mixture, as reported previously[16].

Transient co-transfection of S2 cells

S2 cells (catalogue number CRL-1963, ATCC) were maintained at 27 °C in 90% Schneider's *Drosophila* medium (catalogue number 21720024, ThermoFisher) supplemented with 10% heat-inactivated fetal bovine serum (catalogue number F4135, Sigma), as reported previously[16]. pAC5.1 vectors of CLIP–CryΔ and Tim–SNAP–HA–ALFA were delivered into S2 cells using the TransIT-Insect Transfection Reagent (catalogue number MIR6100, Mirus) following a modified version of the manufacturer's instructions. Briefly, about twenty 100-mm culture dishes (catalogue number 353003, Corning) with $1{,}000 \times 10^4$ cells in 10 ml fresh growth medium were prepared on day 1. About 20 h later, 10 μg DNA in total (CryΔ/Tim mass ratio 1:1) were transfected by the TransIT-Insect reagent in each 100-mm dish. At 72 h after transfection, cells were collected by centrifugation at 500*g* for 5 min at room temperature, washed once with chilled PBS and then stored at −80 °C until lysis.

Nanobody-based affinity purification of the Cry–Tim complex

Two cycles of freeze–thaw were used to lyse the S2 cells as follows: S2 cell pellets from 200 ml of culture were resuspended with 16 ml lysis buffer (50 mM Tris, pH 8, NaCl 150 mM, 20% glycerol, 1× protease inhibitor (catalogue number A32965, ThermoFisher)), divided as 800-μl aliquots in each tube and flash frozen in liquid nitrogen. The 800-μl aliquots were then quickly thawed in a room-temperature water bath. The lysate aliquots were resupended (without vortexing) and the freeze–thaw cycle was repeated. A 100 U ml^{-1} quantity of benzonase (sc-202391, Santa Cruz Biotechnology) was added to the sample and incubated at 4 °C for 45 min to remove DNA and RNA contamination. The cell lysate was spun at 20,000*g* for 20 min at 4 °C and further filtered with a 0.45-μm PVDF syringe filter (catalogue number SLHV033NB, Millipore Sigma). A 320 μl volume of ALFA resin 50% slurry (catalogue number N1512, Nanotag Biotechnologies) was equilibrated with lysis buffer and then incubated with the cell lysate at 4 °C for 1 h on an end-to-end rotator (catalogue number 88881001, ThermoFisher). The slurry was transferred to a 15-ml Falcon tube and centrifuged at 1,000*g* for 1 min, and the resin was washed with 7 ml wash buffer (HEPES 50 mM, pH 7.9, NaCl 150 mM, 10% glycerol). This process was repeated three times. Then the resin was resuspended in 1 ml wash buffer and split into two and applied to separate spin columns (catalogue number 6572, Bio-Vision), with 80 μl resin applied to each column. The spin columns were washed four times with 500 μl wash buffer and spun down at 1,000*g*. An 80 μl volume of resin in each spin column was resuspended in 500 μl elution buffer (wash buffer with 200 μM ALFA peptide; catalogue number N1520, Nanotag Biotechnologies) and incubated in a cold room for 20 min on an end-to-end rotator. The columns were spun at 1,000*g* for 1 min to collect the eluate. The elution was repeated three times and all of the eluted samples were then combined (3 ml in total).

DSSO crosslinking coupled with size-exclusion chromatography

The eluate was concentrated to about 70–80 μl (while maintaining the final protein concentration at less than 2 mg ml^{-1} to ensure efficient crosslinking) with a 30-kDa Vivaspin concentrator (catalogue number 28932235, Cytiva). A 50 mM stock solution of DSSO (catalogue number A33545, ThermoFisher or catalogue number 9002863, Cayman Chemicals) was prepared in dimethylsulfoxide. DSSO was added to the elution sample to a final concentration of 1 mM and incubated at room temperature for 45 min, followed by quenching for 5 min at room temperature with addition of 1 M Tris buffer (pH 8) to produce a final concentration of 20 mM Tris. The crosslinked complex was concentrated by 50-kDa-cutoff Vivaspin (catalogue number 28932236, Cytiva) and purified by a Superose size-exclusion chromatography (SEC) column 6 10/300 (catalogue number 29091596, Cytiva) or 3.2/300 (catalogue number 29091598, Cytiva). The protein complex was eluted in SEC buffer (20 mM HEPES, pH 7.9, 150 mM NaCl) and concentrated to about 40 μl by a 50-kDa-cutoff Vivaspin concentrator.

Crosslinking mass spectrometry

SEC-purified crosslinked product was mixed with 4× Laemmli sample buffer (catalogue number 1610747, BioRad) and 2.5% 2-mercaptoethanol (BME, catalogue number 1610710, BioRad) and then boiled for 6 min. The sample was then loaded on an SDS–PAGE gel and stained with QC colloidal Coomassie stain (catalogue number 1610803, BioRad). The band of the complex (about 20 μg protein sample) was cut out and prepared for MS–MS analysis of crosslinked peptides as previously reported[51] and described below.

In-gel digestion of SDS gel bands

The protein band (about 20 μg protein) was sliced into about 1-mm cubes. The excised gel pieces were washed consecutively with 400 μl deionized water followed by 50 mM ammonium bicarbonate, 50% acetonitrile and finally 100% acetonitrile. The dehydrated gel pieces were reduced with 200 μl of 10 mM dithiothreitol (DTT) in 100 mM ammonium bicarbonate for 45 min at 56 °C, followed by alkylation with 200 μl of 55 mM iodoacetamide in 100 mM ammonium bicarbonate at room temperature in the dark for 45 min. Wash steps were repeated as described above. The gel was then dried and rehydrated with 100 μl LysC at 10 ng μl^{-1} in 50 mM ammonium bicarbonate containing 10% acetonitrile and incubated at 37 °C for 3 h. After the 3 h incubation, 30 μl trypsin at 43 μg μl^{-1} in 50 mM ammonium bicarbonate was added and the sample was incubated at 37 °C for a further 18 h. The digested peptides were extracted from the gel twice with 200 μl of 50% acetonitrile containing 5% formic acid and once with 200 μl of 75% acetonitrile containing 5% formic acid. Extractions from each sample were pooled together and then divided equally in half. One half was then filtered with a 0.22-μm spin filter (Costar Spin-X from Corning), dried to dryness in a speed vacuum and analysed as LysC–trypsin digests. The second half was dried to dryness in a speed vacuum, reconstituted with 30 μl GluC at 33 ng μl^{-1} in 50 mM ammonium bicarbonate (pH 7.9), and incubated at 37 °C for 18 h. After incubation, formic acid was added to stop the enzyme reaction. The digests were filtered with a 0.22-μm spin filter, dried to dryness in a speed vacuum and analysed as LysC–trypsin–GluC digests. Each sample was reconstituted in 0.5% formic acid before LC–MS/MS analysis.

Crosslink identification by nanoLC–MS/MS

The digested product was characterized by nanoLC–MS/MS analysis at the Cornell Biotechnology Resource Center. The analysis was carried out using an Orbitrap Fusion Tribrid (ThermoFisher) mass spectrometer equipped with a Nanospray Flex ion source, and coupled with a Dionex UltiMate 3000 RSLCnano system (ThermoFisher). Each sample was loaded onto a nano Viper PepMap C18 trapping column (5 μm, 100 μm × 20 mm, 100 Å, ThermoFisher) at 20 μl min^{-1} flow rate for rapid sample loading. After 3 min, the valve was switched to allow peptides to be separated on an Acclaim PepMap C18 nano column (2 μm, 75 μm × 25 cm, ThermoFisher) at 35 °C in a 90-min gradient of 5% to 40% buffer B (98% acetonitrile with 0.1% formic acid) at 300 nl min^{-1}. The Orbitrap Fusion was operated in positive ion mode with nano spray voltage set at 1.7 kV and source temperature at 275 °C. External calibrations for Fourier transform, ion-trap and quadrupole mass analysers were carried out before the analysis. Samples were analysed using the CID–MS^2–MS^3 workflow, in which the MS scan range was set to 375–1,500 m/z and the resolution was set to 60,000. Precursor ions with charge states 3–8 were selected for CID–MS^2 acquisitions in an Orbitrap analyser with a resolution of 30,000 and an AGC target of 5×10^4.

The precursor isolation width was 1.6 *m/z* and the maximum injection time was 100 ms. The CID–MS^2 normalized collision energy was set to 25%. Targeted mass-difference-triggered HCD–MS^3 spectra were acquired in the ion trap with an AGC target of 1×10^4. When a unique mass difference (Δ = 31.9721 Da) was observed in CID–MS^2 spectra for ions with a single charge and multiple charges, the HCD collision energy at 38% and 28% was used respectively, for the subsequent MS^3 scans. All data were acquired under Xcalibur 4.3 operation software and Orbitrap Fusion Tune application v3.4 (ThermoFisher).

MS data analysis

All MS, MS^2 and MS^3 raw spectra from each sample were searched using Proteome Discoverer 2.4 (ThermoFisher) with the XlinkX v2.0 algorithm for identification of crosslinked peptides. The search parameters were as follows: four missed cleavages for either double digestion or triple digestion with a fixed carbamidomethyl modification of cysteine, variable modifications of methionine oxidation, asparagine and glutamine deamidation, and protein N-terminal acetylation. The peptide mass tolerance was 10 ppm, and the MS^2 and MS^3 fragment mass tolerance was 20 ppm and 0.6 Da, respectively. The *D. melanogaster* database with added targeted protein sequences was used for the Proteome Discoverer 2.4 database search with a 1% false discovery rate for reporting of crosslink results. Identified crosslinked peptides were filtered for maximum XlinkX score > 40 containing at least two identified MS^3 spectra for each pair of crosslinked peptides. Search results were exported by the software as a spreadsheet. The crosslinked peptides were analysed by xiNET to generate the map of inter or inner crosslinks between the two target proteins.

SWFTI assay

S2 cells were co-transfected as described above with pAC 5.1 vectors of CLIP–Cry(377L) and Tim–SNAP–HA–ALFA variants at a mass ratio of 3:1. The pulldown assay was carried out as follows, using a method similar to that previously described[16]. A 400 µl volume of lysis buffer containing non-ionic detergent (50 mM Tris buffer, pH 8, 150 mM NaCl, 1% IGEPAL CA-630 (catalogue number I8896, Sigma Aldrich), 10% glycerol and 1× protease inhibitor (catalogue number A32965, ThermoFisher)) was added to cell pellets collected from 5 ml S2 cells. EDTA was omitted to avoid disturbing SNAP and CLIP dye labelling. The pH of all buffers was adjusted at the working temperature. After cells were incubated with lysis buffer on ice for 30 min (flicking the tube every 10 min to avoid vortexing), cell debris was removed by spinning at 15,000*g* for 15 min at 4 °C.

To label the lysate sample with SNAP or CLIP dyes, 1 part lysate was diluted with 2 parts labelling buffer (50 mM Tris buffer, pH 8, 150 mM NaCl, 10% glycerol) to decrease the concentration of non-ionic detergent to less than 0.5%, as recommended by the manufacturer (New England Biolabs). Then 27 µl of diluted lysate was mixed with 1 µl of 0.1 mM SNAP dye (catalogue number S9102S, SNAP-Cell 647-SiR), 1 µl of 0.1 mM CLIP dye (catalogue number S9217S, CLIP-Cell 505) and 1 µl of 30 mM DTT and incubated in the dark at room temperature for 1 h. A 10 µl volume of 4× Laemmli sample buffer (catalogue number 1610747, BioRad) and 1.5 µl BME was added to the 30 µl mix, boiled at 95 °C for 5 min. After labelling with the SNAP or CLIP substrate, the sample was protected from bright light to avoid photobleaching. A 20 µl volume of the sample was loaded on a gradient stain-free gel (catalogue number 4568095, BioRad) to carry out SDS–PAGE. The result was imaged with Chemidoc (BioRad) and quantified by image lab software (BioRad).

To label Cry and Tim on the affinity resin, about 350 µl cell lysate was mixed with 10 µl pre-washed magnetic HA resin slurry (catalogue number 88836, ThermoFisher) and incubated on an end-to-end rotator overnight at 4 °C. The dark sample was covered by foil and kept in the dark. The next day, the resin was washed with room temperature 500 µl TBS-T (20 mM Tris buffer, pH 7.6, 150 mM NaCl, 0.05% Tween-20) four times. Then the HA resin was resuspended in 27 µl labelling buffer, 1 µl of 0.1 mM SNAP dye, 1 µl of 0.1 mM CLIP dye and 1 µl of 30 mM DTT. The tube was incubated in the dark on an end-to-end rotator at room temperature for 1 h. Subsequently, 10 µl of 4× Laemelli sample buffer and 1.5 µl BME were added to the 30 µl resin mix. The tube was boiled at 95 °C for 10 min to denature and elute Cry and Tim from HA resin. SDS–PAGE and imaging were carried out as described above. Effective K_d values were calculated as described elsewhere[16].

Negative-stain electron microscopy

Initial Cry–Tim samples were screened by negative-stain electron microscopy. Formvar- and carbon-coated 200 mesh copper grids (Electron Microscopy Sciences) were plasma cleaned by the GloQube glow discharge system (Electron Microscopy Sciences). A 10 µl volume of 0.05 mg ml^{-1} Cry–Tim solution was applied onto the grid, incubated for 30 s, and the excess solution was blotted with filter paper. A 10 µl volume of 2% uranyl acetate was then applied to the grid twice for 30 s of incubation followed by blotting. The grid was air-dried for 5 min and visualized using a Philips Morgagni 268 transmission electron microscope at 100 keV.

Cryo-EM grid preparation and data collection of Cry–Tim complex

A 4 µl volume of 0.5 mg ml−1 Cry–Tim solution was applied to glow-discharged grids (300 mesh Quantifoil Au, R1.2/1.3) that were purchased from Electron Microscopy Sciences. After 30 s of incubation, the excess solution was blotted for 4 s with filter paper by a Vitrobot Mark IV (ThermoFisher). Grids were subsequently vitrified in liquid ethane and stored in liquid nitrogen. Cryo-EM images of the Cry–Tim complex were collected on a Talos Arctica (ThermoFisher) operated at 200 keV at a nominal magnification of ×79,000 with a Gatan GIF Quantum LS Imaging energy filter, using a Gatan K3 direct electron camera in super-resolution counting mode, corresponding to a pixel size of 0.516 Å. A total of 1,636 images stacks were obtained with a defocus rage of −0.8 to −2.0 µm by EPU (ThermoFisher). Each stack video was recorded for a total dose of 53 electrons per square ångström.

Cryo-EM data processing of the Cry–Tim complex

Dose-fractionated image stacks were subjected to motioncor2 (ref. 52) wrapped in Relion 3.1.3 (ref. 53) followed by patch CTF estimation in CryoSparc v3.2.0 (ref. 54). The micrographs whose CTF estimation is greater than 4 Å were selected for later processing, which yielded 1,473 micrographs. Blob picker in CryoSparc was used on the 300 randomly selected micrographs, which was followed by two-dimensional classification and generation of about 23,000 particles for the first-round Topaz train[55]. Then the trained model was applied to all 1,473 micrographs and about 48,000 particles were extracted and selected by two-dimensional classification for the second round of Topaz train particle identification. After two rounds of Topaz train and extraction, in total about 2 million particles were picked. Following two-dimensional classification non-relevant particles were removed and only the best classes were kept (about 350,000 particles). The particle stack was subjected to Bayesian polishing in RELION 3.1.3 and imported back to CryoSparc for the further ab initio reconstruction and heterogeneous refinement with three classes. The second and third classes were selected, and multiple rounds of homogeneous and non-uniform refinement were carried out to yield a global 3.48 Å (about 98,000 particles) and a global 3.3 Å (about 160,000 particles) map using 'gold standard' FSC at 0.143 cutoff, respectively. The 3.3 Å map is subjected to the model building. C_1 symmetry was used throughout data processing. The workflow is shown in Extended Data Fig. 1.

Model building and refinement of the Cry–Tim complex

The initial Cry model was adapted from the PDB entry 4GU5, and the initial Tim model was fetched from AlphaFold Protein Structure Database entry P49021 (ref. 32). Both models were manually docked into

the map by UCSF ChimeraX[56]. The model was subjected to ISOLDE[57] to fit the loops that undergo conformational changes into the map density. Intrinsically disordered loops of Tim that were not visualized in the map were not included in the model. The Cry–Tim model was subjected to multiple rounds of automatic refinement using Phenix real-space refinement, and manual building using Coot[58–60]. Validation was carried out by MolProbity[61]. The final refinement statistics are provided in Supplementary Table 1.

The unassigned polypeptide in the Tim groove was built in both directions and the sequence register shifted along the backbone one residue at a time for a 150-residue stretch in the 250–400 range. Each sequence register was real-spaced refined against the electron density and the associated *Q*-score[62] was calculated. Given the helical nature of the density at one end of the groove, directionality of the sequence was best fitted with the polypeptide having its N-terminal end closest to Cry and the C-terminal end running towards the Lys313 and Lys328 crosslinking partners at the base of the groove. Side-chain density in the helical region showed a variable size pattern that was inconsistent with the repetitive patterns of much of the disordered region beyond residue 350. C-terminal to the groove peptide Lys313 and Lys328 are unresolved, but should be closely positioned to their crosslinking partners. To assign sequence to the disconnected Tim helix binding the PHR C terminus, secondary structure predictions on the regions of Tim not resolved in the ordered core were carried out by RAPTORX[63]. All predicted helical sequences were fitted into the density and refined in real space with a range of sequence registers. As a further check, AlphaFold2.1 (ref. 32) was used to predict interactions between Cry and the disordered region of Tim, with the highest scoring predictions also tested for agreement with the electron density map. The disconnected helix exhibits strong side-chain density, which sets its directionality and ruled out many sequence placements. Given the resolution limitations of the cryo-EM maps, we consider the sequence assignments of both of these helical regions provisional.

Analysis of Tim structural homologues

Structural comparisons and sequence alignments of Tim structural homologues were carried out with the DALI server[64].

Reporting summary

Further information on research design is available in the Nature Portfolio Reporting Summary linked to this article.

Data availability

The cryo-EM density maps and the atomic model for Tim–Cry have been deposited in the Electron Microscopy Data Bank (EMD-27335) and the PDB (8DD7), respectively. The mass spectrometry proteomics data have been deposited to the ProteomeXchange Consortium through the PRIDE partner repository with the dataset identifier PXD034054. All other data are contained within the Supplementary Information. Reagents are available from the authors upon request.

Code availability

No custom computer code was used in the study.

51. Muok, A. R. et al. Engineered chemotaxis core signaling units indicate a constrained kinase-off state. *Sci. Signal.* **13**, eabc1328 (2020).
52. Zheng, S. Q. et al. MotionCor2: anisotropic correction of beam-induced motion for improved cryo-electron microscopy. *Nat. Methods* **14**, 331–332 (2017).
53. Scheres, S. H. RELION: implementation of a Bayesian approach to cryo-EM structure determination. *J. Struct. Biol.* **180**, 519–530 (2012).
54. Punjani, A., Rubinstein, J. L., Fleet, D. J. & Brubaker, M. A. cryoSPARC: algorithms for rapid unsupervised cryo-EM structure determination. *Nat. Methods* **14**, 290–296 (2017).
55. Bepler, T. et al. Positive-unlabeled convolutional neural networks for particle picking in cryo-electron micrographs. *Nat. Methods* **16**, 1153–1160 (2019).
56. Pettersen, E. F. et al. UCSF ChimeraX: structure visualization for researchers, educators, and developers. *Protein Sci.* **30**, 70–82 (2021).
57. Croll, T. I. ISOLDE: a physically realistic environment for model building into low-resolution electron-density maps. *Acta Crystallogr. D* **74**, 519–530 (2018).
58. Morin, A. et al. Collaboration gets the most out of software. *Elife* **2**, e01456 (2013).
59. Emsley, P., Lohkamp, B., Scott, W. G. & Cowtan, K. Features and development of Coot. *Acta Crystallogr. D* **66**, 486–501 (2010).
60. Liebschner, D. et al. Macromolecular structure determination using X-rays, neutrons and electrons: recent developments in Phenix. *Acta Crystallogr. D* **75**, 861–877 (2019).
61. Chen, V. B. et al. MolProbity: all-atom structure validation for macromolecular crystallography. *Acta Crystallogr. D* **66**, 12–21 (2010).
62. Pintilie, G. et al. Measurement of atom resolvability in cryo-EM maps with Q-scores. *Nat. Methods* **17**, 328–334 (2020).
63. Kallberg, M. et al. Template-based protein structure modeling using the RaptorX web server. *Nat. Protoc.* **7**, 1511–1522 (2012).
64. Holm, L. & Laakso, L. M. Dali server update. *Nucleic Acids Res.* **44**, W351–W355 (2016).

Acknowledgements We thank Q. Fu and S. Zhang of the Proteomics and Metabolomics Facility of Cornell University for providing the mass spectrometry data; K. Spoth and M. Silvestry-Ramos for help with electron microscopy instrumentation; Y. Li for suggesting use of the ALFA tag and experimental assistance; G. Merz, T.-T. Nguyen and C. Aplin for general aid; and R. Cerione and M. Young for helpful feedback. Figure 1a, the inset in Fig. 2b, Fig. 4d and Supplementary Fig. 1 were created with BioRender.com. This work was supported by NIH grants R35GM122535 to B.R.C. and 1S10 OD017992-01 for the Orbitrap Fusion mass spectrometer. This work made use of the Cornell Center for Materials Research Shared Facilities that are supported through the NSF (DMR-1719875).

Author contributions All authors contributed to each aspect of the study, but primarily, C.L. and C.C.D. developed the SWFTI assay; C.L. carried out Cry–Tim binding assays; C.L. assisted by C.C.D. developed methods to produce the Cry–Tim complex; C.L. prepared the complex for structural analysis; S.F. prepared samples for cryo-EM, and collected and processed cryo-EM data; S.F. and B.R.C. built the Cry–Tim model; C.L., S.F. and B.R.C. analysed the structure; C.L., S.F., C.C.D. and B.R.C. wrote the manuscript; B.R.C. conceived of and oversaw the project.

Competing interests The authors declare no competing interests.

Additional information

Supplementary information The online version contains supplementary material available at https://doi.org/10.1038/s41586-023-06009-4.

Correspondence and requests for materials should be addressed to Brian R. Crane.

Peer review information *Nature* thanks Amita Sehgal, Sebastian Westenhoff and the other, anonymous, reviewer(s) for their contribution to the peer review of this work. Peer reviewer reports are available.

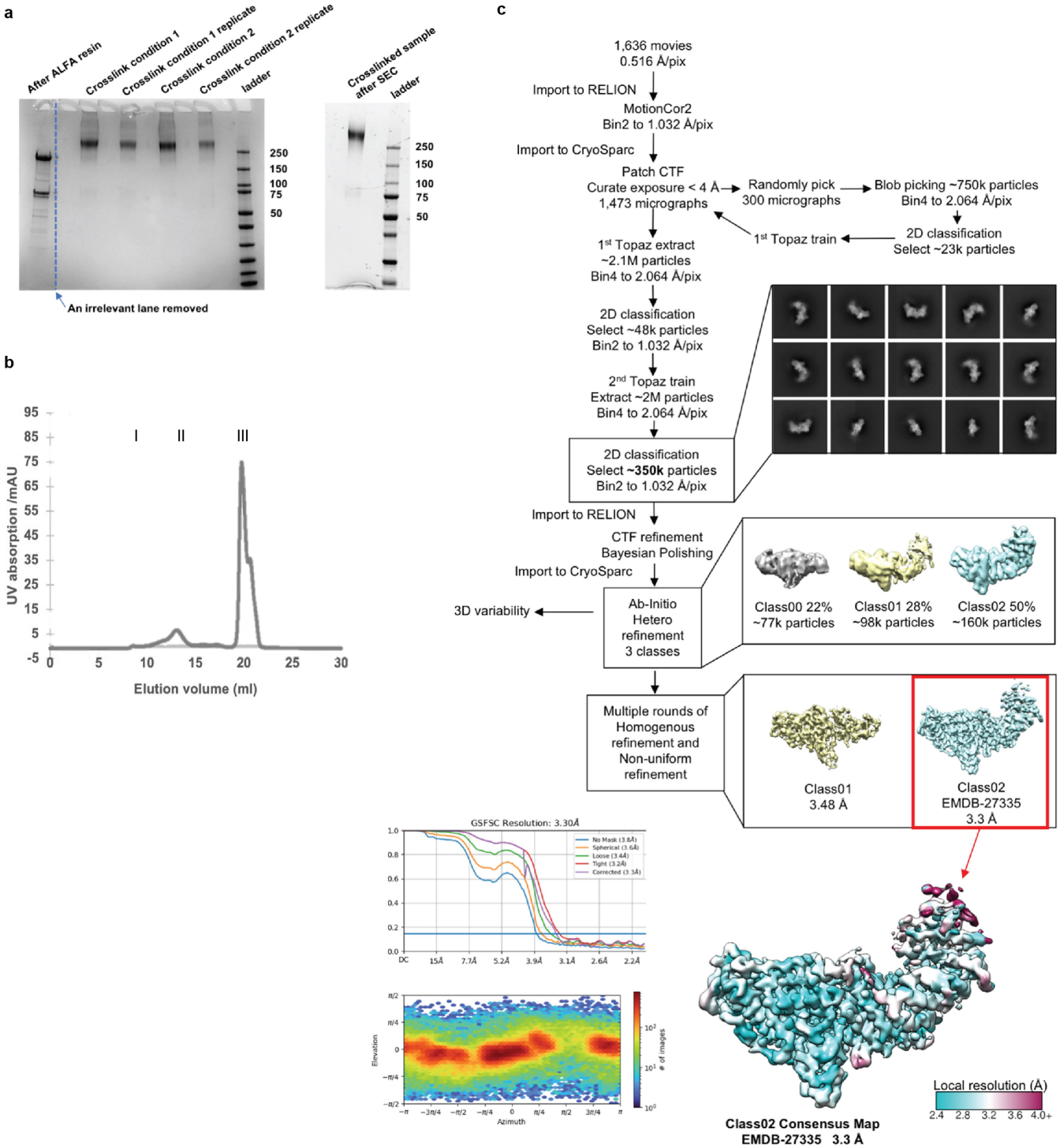

Extended Data Fig. 1 | Cry-Tim purification and cryo-EM workflow. Purification of Cry-Tim complexes for cryo-EM. (a) SDS-PAGE gel showing complex after elution from the ALFA resin, followed by crosslinking, followed by SEC. (b) SEC trace of purified complex, peak I: aggregates, peak II: Cry-Tim complex, and peak III: excessive ALFA peptide. (c) Processing workflow for Cry-Tim collected on a Talos Arctica (Thermo Fischer Scientific) operated at 200 keV using a Gatan K3 direct electron camera. The red box indicates the final reconstruction in this study. Data processing was carried out in CryoSparc and RELION. Motion Correction was performed by RELION (MotionCor2); with Contrast Transfer Function (CTF) applied in CryoSparc. Topaz was used for particle classification. Overall resolution determination in CryoSparc by Gold Standard Fourier Shell Correlation (GSFSC) is shown at the mid-bottom left. Corrected values give 3.30 Å overall resolution. Local resolution exceeds 2.5 Å, as shown on the bottom right. Particle orientational sampling is reasonably uniform as shown at the bottom left. Number of particles (images) holding a given azimuthal and elevation angle are indicated in the 2-dimensional histogram.

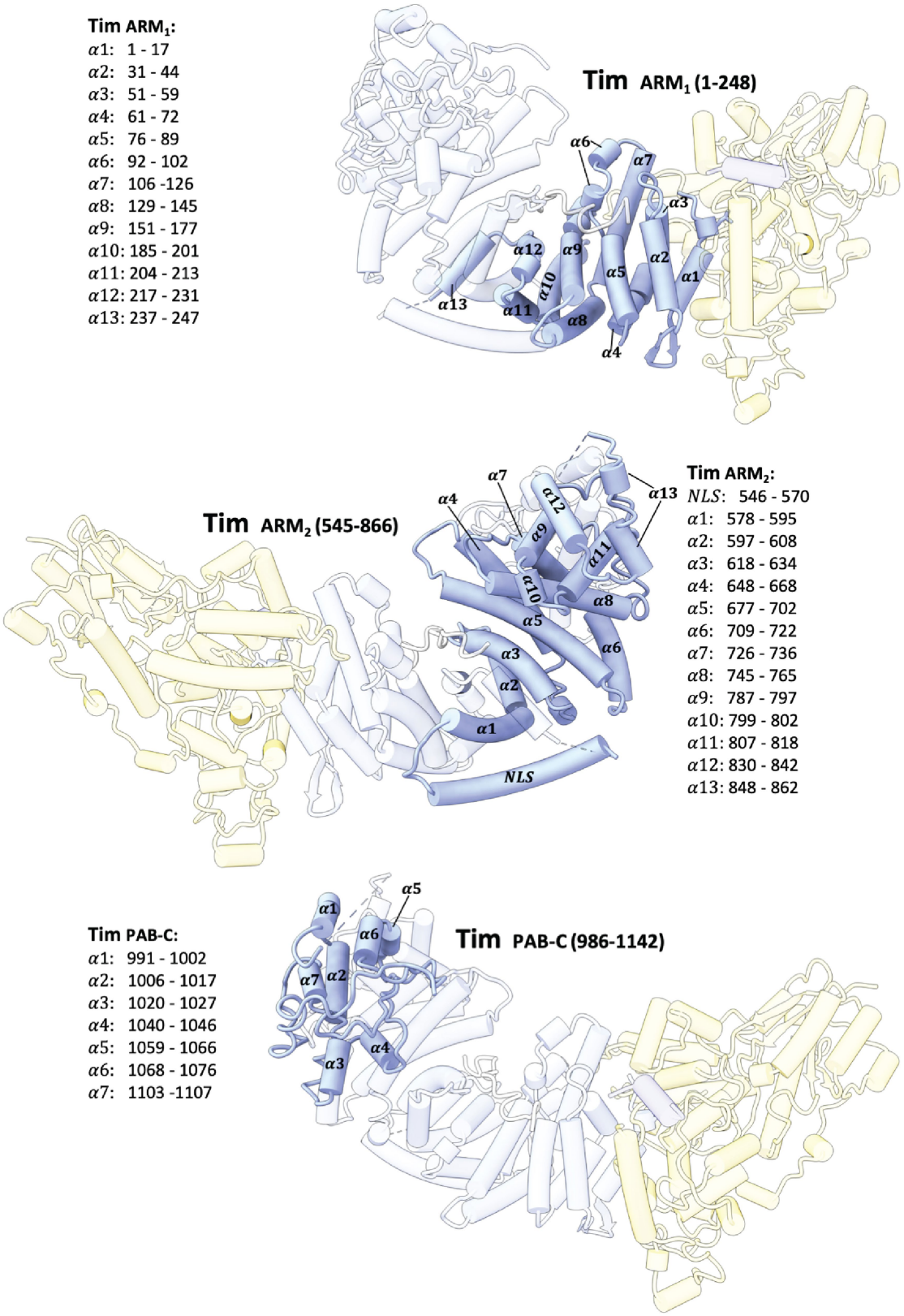

Extended Data Fig. 2 | Tim domain construction and secondary structure assignments. Domain construction and secondary structure assignments of Tim.

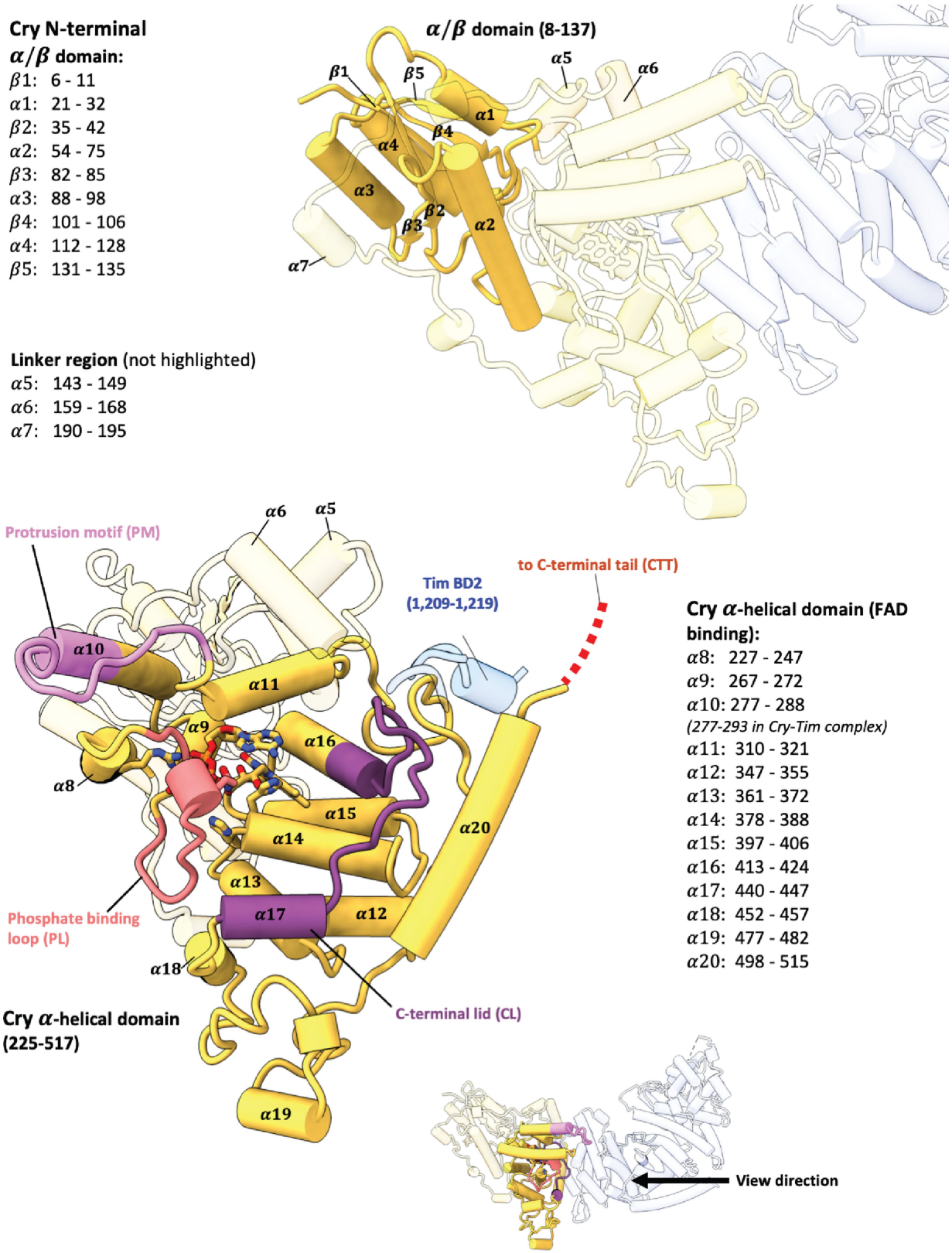

Extended Data Fig. 3 | Cry domain construction and secondary structure assignments. Domain construction and secondary structure assignments of Cry.

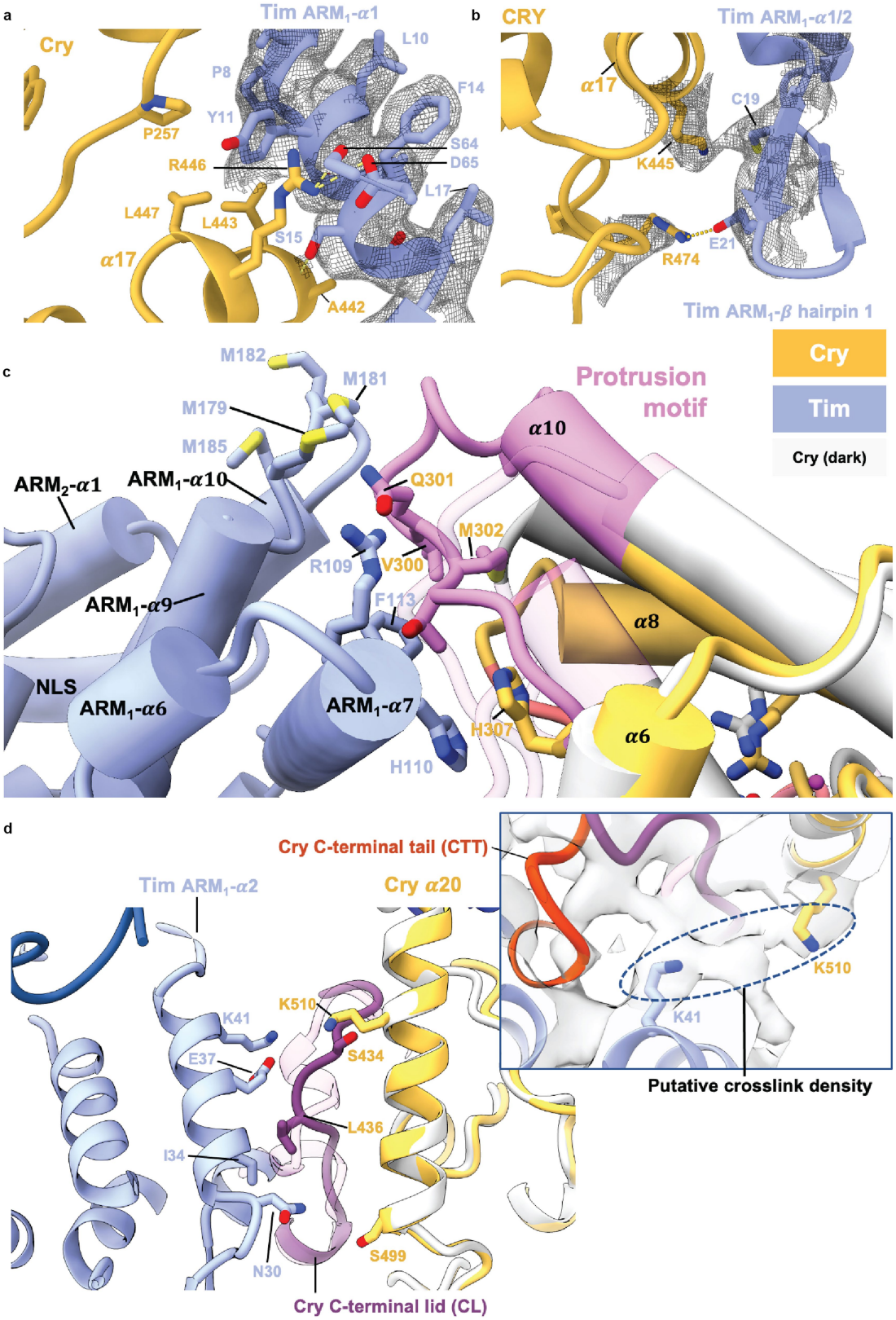

Extended Data Fig. 4 | See next page for caption.

Extended Data Fig. 4 | Key interactions at the Cry-Tim interface. (a) Interactions between the bottom half of Tim ARM_1-α1 with Cry. ARM1-α1 binds across Cry α14 and α17. The guanidinium of Cry R446 (on α17) forms π-cation interaction with Tim Y11. Tim Y11 participates in hydrophobic contacts with Cry P257, L443 and L447. On Tim α1, Tim P8 stacks against Cry α12 and Tim S15 hydrogen bonds to the backbone carbonyl of Cry A442. (b) In the β-hairpin connecting ARM_1-α1 to ARM_1-α2 E21 salt-bridges to R474 and C19 interacts with K445. (c) Interactions of the Cry protrusion motif. Tim R109, F113, and H110 interact with the protrusion motif of Cry. Tim ARM_1-α7 H110 stacks with Cry H307. Four Met residues (M179, M181 M182, M185) in the ARM_1-α9-α10 loop provide side-chain interactions with the tip of the Cry protrusion motif. The Cry α10 helix lengthens to residue A295 compared to the dark state and the following 300–306 residues interact directly with ARM_1-α10. (d) Interactions of the Cry C-terminal lid and α20 helix. The restructured C-terminal lid interacts with residues on Tim ARM_1-α2. For examples, I34 make a hydrophobic contact with I436 and E37 hydrogen bonds to the backbone of S434. At the end of ARM_1-α2, Asn30 contacts the N-terminal end of Cry α20. A DSSO crosslink observed between Lys510 on Cry α20 and Lys41 on ARM1-α3 is fully consistent with the observed interface.

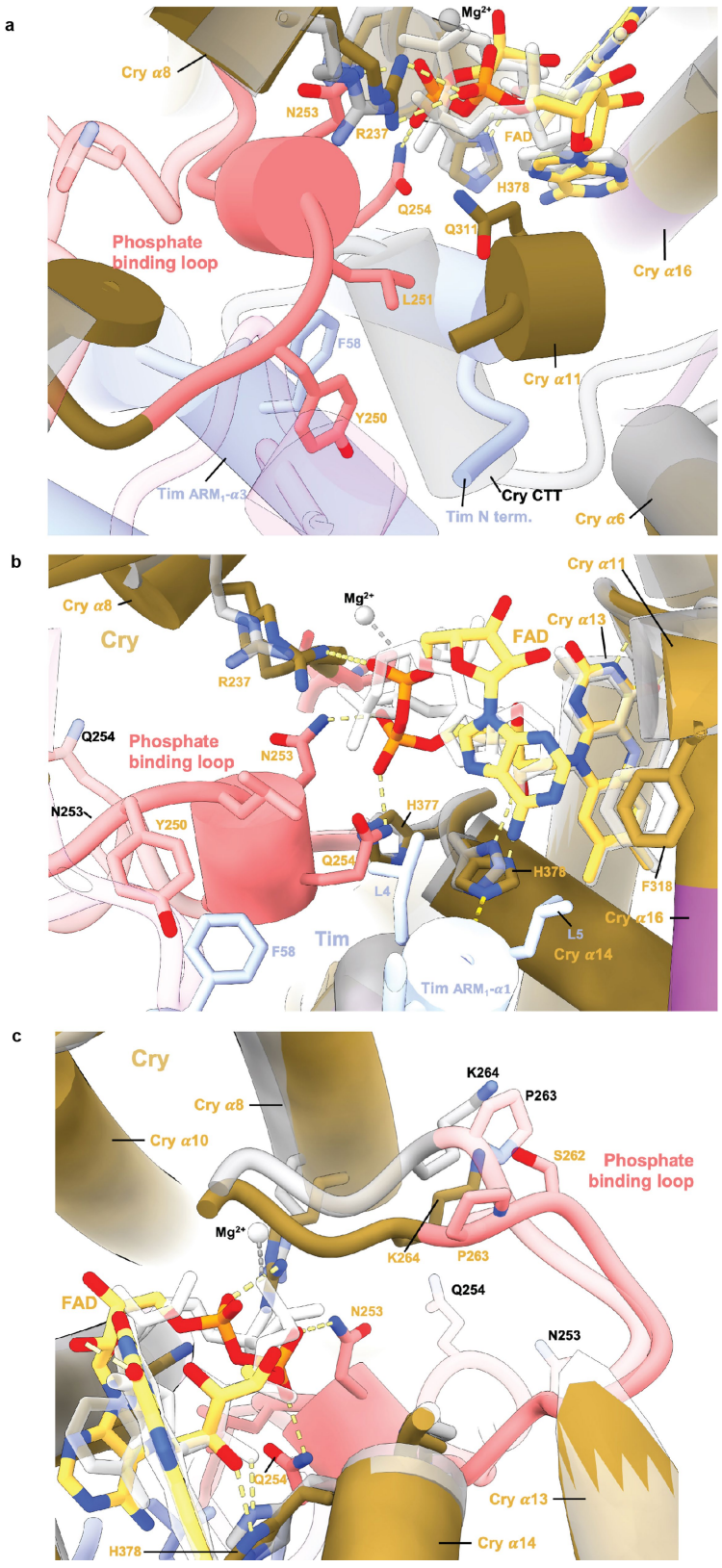

Extended Data Fig. 5 | Changes in flavin binding pocket for Cry dark and bound states. Comparison of the flavin pocket in Cry-Tim compared to in dark-state Cry (PDB 4GU5). (a) In Cry-Tim, Y250 and L251 interact with the FAD pocket and make space for the top of Tim ARM$_1$-α3 to insert F58 behind the new conformation of the phosphate-binding loop. Q311 swivels away from Tim L4. (b) The FAD adenine ring of Cry-Tim shifts 1.5 Å relative to the unbound structure. Cry F318 shifts away from its original position and harbors helix α11 to compensate for the FAD adenine ring adjustment, following the protrusion motif. (c) Q. New diphosphate conformations couple to rearrangement of the Cry 262-to-265 loop.

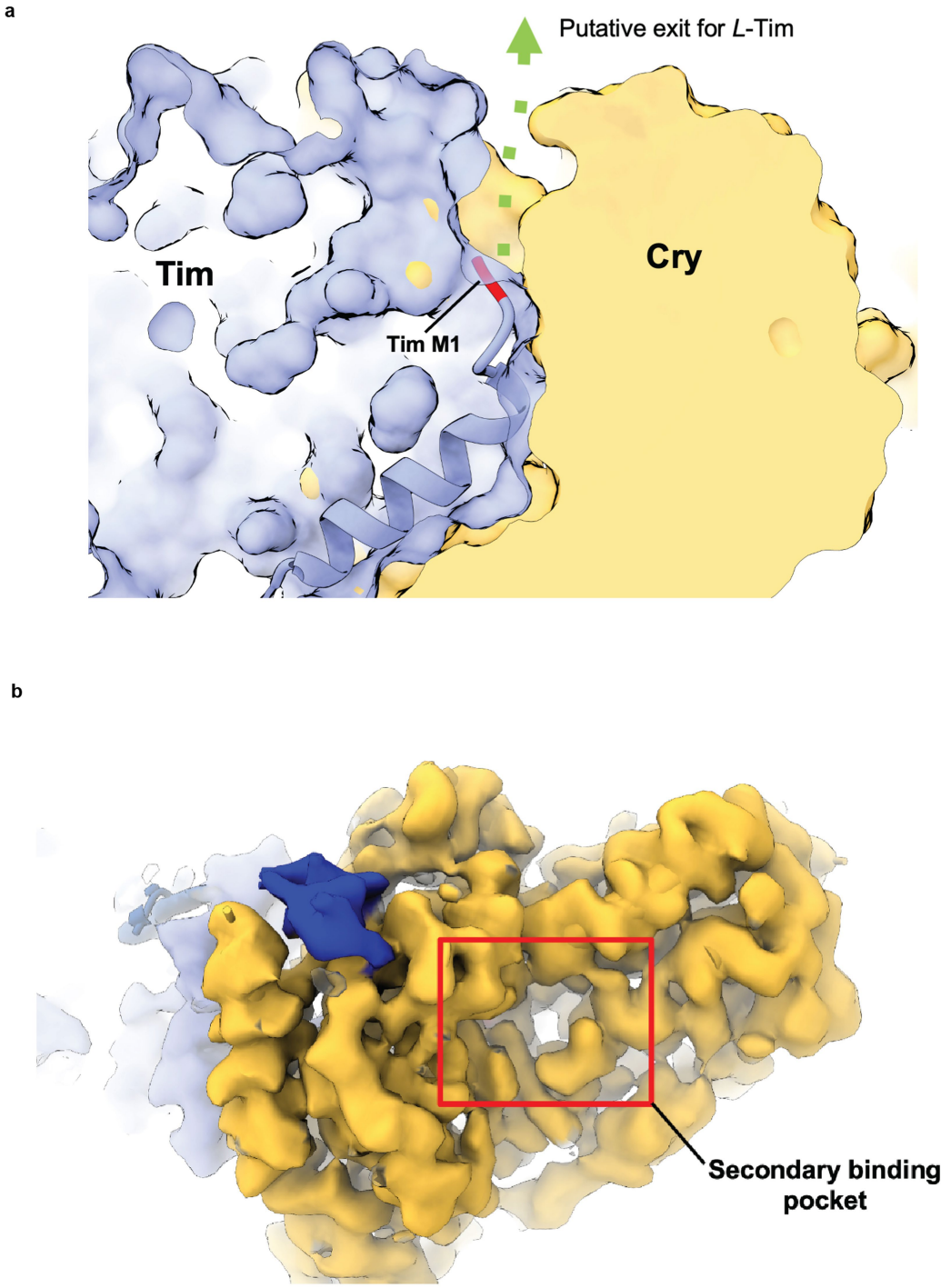

Extended Data Fig. 6 | Exit channel at the Cry-Tim interface and Cry secondary pocket. (a) Putative exit channel for the additional 23 N-terminal residues of L-Tim. The first residue of Tim (M1) is colored as red. A solvent accessible channel at the interface between the two proteins is marked as the green arrow. (b) Electron density for the secondary binding pocket of CRY where antenna cofactors bind in photolyases and mCRY interact with other clock proteins (**red** box). Cry (**yellow**), Tim (**periwinkle blue**), Tim 1,209–1,219 (**blue**), Tim groove (**navy blue**). Although the pocket is well formed, there is no obvious density for additional moieties.

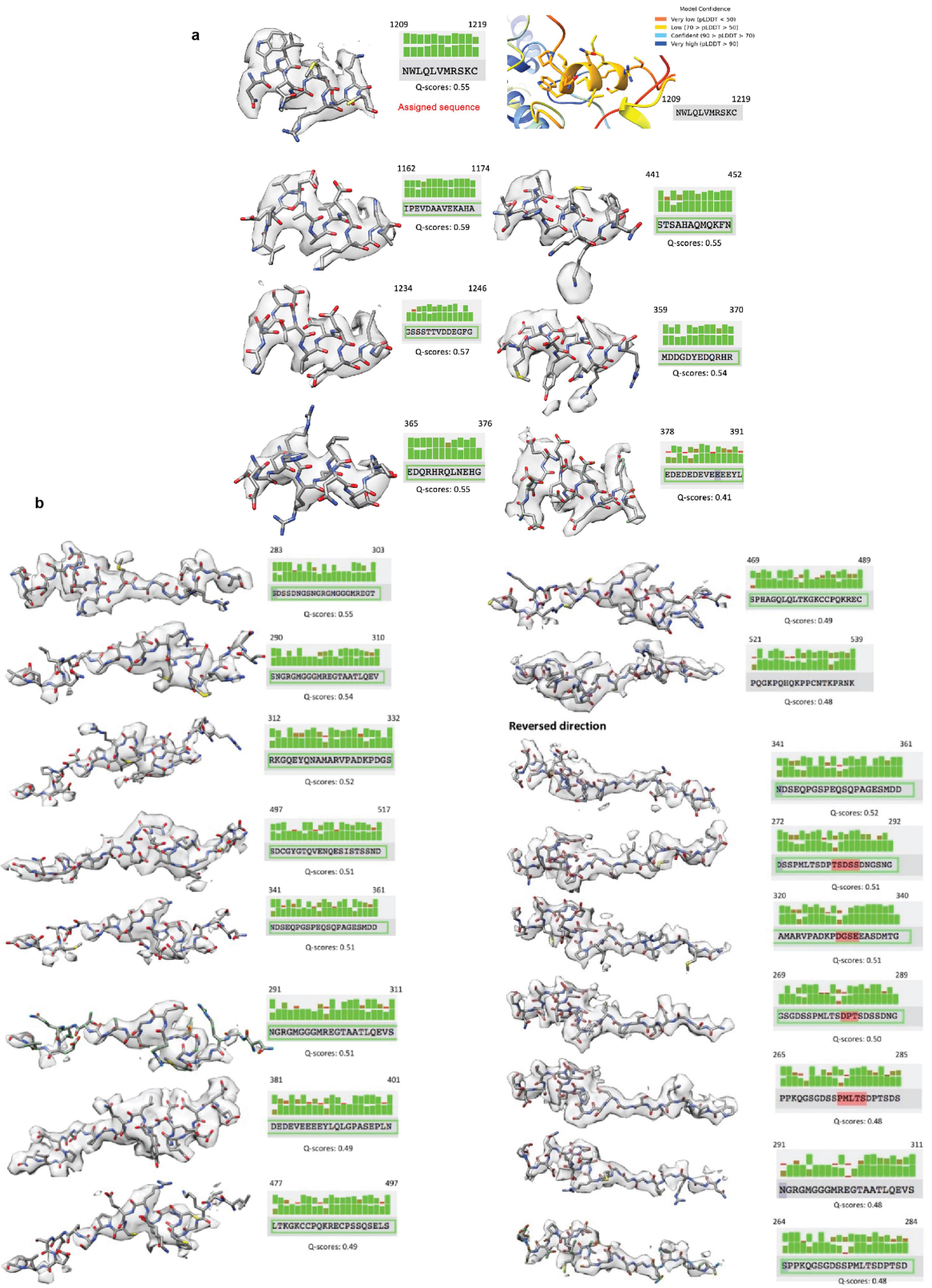

Extended Data Fig. 7 | Tim peripheral helix and groove peptide fitting to the electron density map and associated Q-scores. (a) Real-space electron density fitting metrics for the top scoring sequence assignments for the Tim peripheral helix. Real space density agreements were calculated in Q-scores and are shown above for sidechains and below for mainchains. One of the top scoring segments, residues 1209–1219 (top left) was also predicted by AlphaFold2.1 to interact with Cry at the position of the observed electron density, the model confidence pLDDT scores for this segment are given at the top right. (b) Real-space electron density fitting metrics for the top scoring sequence assignments for the Tim groove-binding polypeptide. Real space density agreements were calculated in Q-scores and are shown above for sidechains and below for mainchains. The Tim groove binding polypetide was tested in both directions.

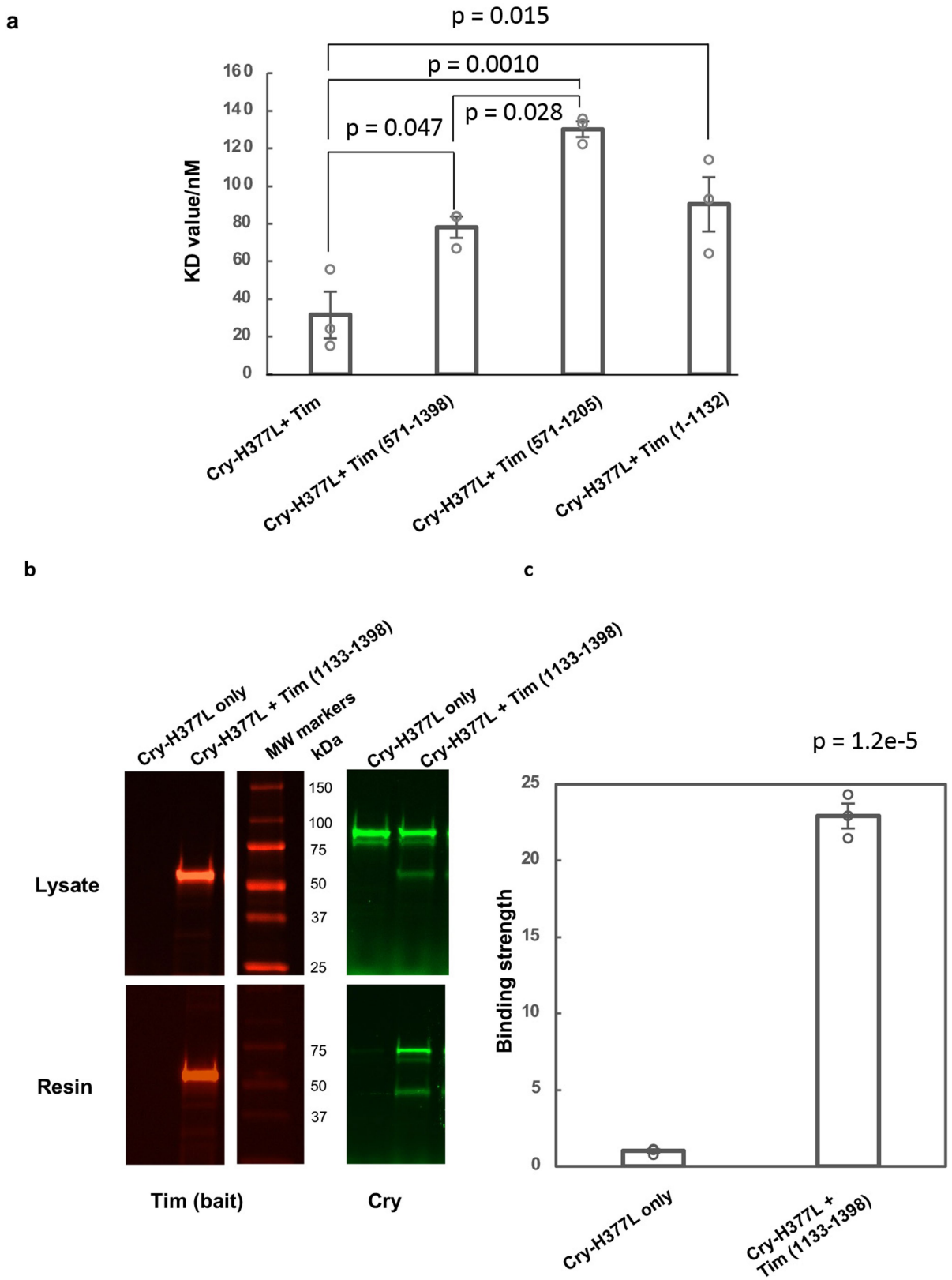

Extended Data Fig. 8 | Relative binding affinities between fragments of Tim and Cry H377L by the SWFTI assay. (a) The Cry H377L variant acts as a constitutive light-activated state and enhances binding affinity for Tim by stabilizing the Tim-binding conformation of Cry[16]. H377L thereby increases Tim expression levels and facilitates detection of weaker binding variants. Mean ± standard error is shown for sample size = 3, from different biological replicates. One-way ANOVA with post-hoc Tukey HSD test was used to determine p values. (b) Pull down results of Cry-H377L with Tim-1133-1398. Cry-H377L interacts with the C-terminal regions of Tim. Gel lanes containing replicates or unrelated samples are not shown. (c) Quantification of the binding strength between Cry-H377L and Tim (1133–1398) compared to the negative control (Cry-H377L only with the same amount of resin). The binding strength is defined as the amount of Cry on the resin divided by the amount of Cry in the lysate sample. The negative control is normalized to 1. Mean ± standard error is shown for sample size = 3, from different biological replicates. Two-tailed unpaired t-test was used to determine p value. Binding affinities could not be derived from this experiment owing to the challenge of producing excessive Cry relative to Tim 1133–1398.

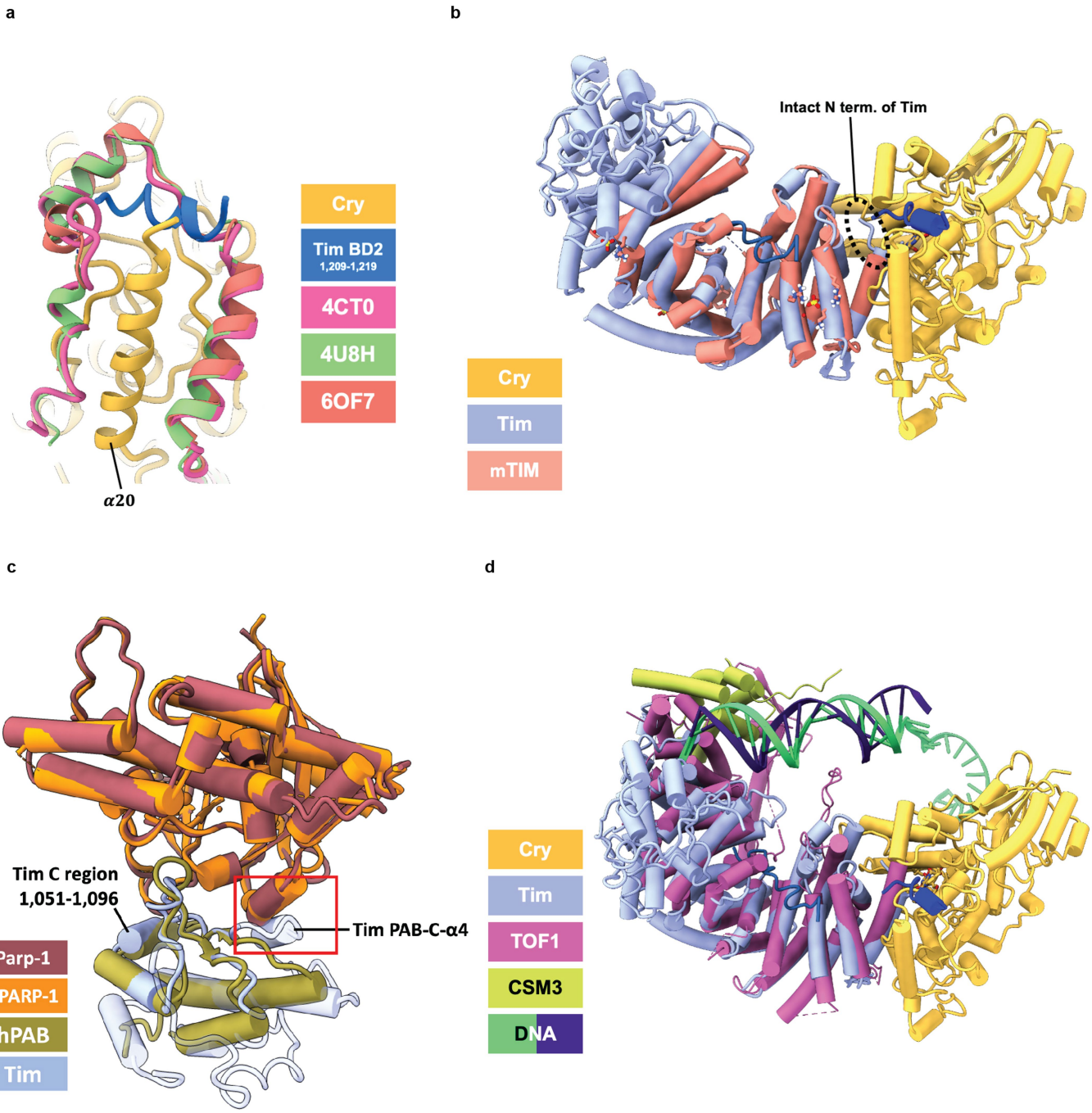

Extended Data Fig. 9 | Comparisons of structural features in the Cry-Tim complex to those of CRY and TIM homologues. (a) Structural comparison of Cry-Tim with mammalian CRY bound with mammalian PER. Tim 1209–1219 (**blue**) follows the backbone trace of mPER (CryΔ (**yellow**), Tim BD2 1209–1219 (**blue**)). 4CT0: Crystal Structure of Mouse Cryptochrome1 in Complex with Period2 (**magenta**). 4U8H: Crystal Structure of Mammalian Period-Cryptochrome Complex (**green**). 6OF7: Crystal structure of the CRY1-PER2 complex (**orange red**). (b) Structural comparison of Cry-Tim (Cry (**yellow**), Tim (**periwinkle blue**), Tim 1209–1219 (**blue**), Tim groove peptide (**navy blue**)) with the crystal structure of the N-terminal domain of human Timeless (PDB ID: 5MQI, **salmon**). Note that mammalian mTIM does not contain the N-terminal residues that bind into the Cry flavin pocket. (c) Structural superposition of Tim PAB (Parp-1 binding) domain and Parp-1 model with the structure of human TIM PAB bound to the PARP-1 catalytic domain (4XHU). Red box highlights the additional Tim *α*-helix (PAB-C-α4) that is incompatible with the interface formed by human PARP-1 and Tim PARP-1 binding. The Tim C region conserved across TIM proteins (residue 1051–1096) is also shown. Tim (this study, **periwinkle blue**), *Drosophila* Parp-1 (AlphaFold2.1 model: **dark red**) 4XHU (PAB:**green**, PARP-1:**orange**). (d) Superposition of Tim and Tof1 within the replisome.

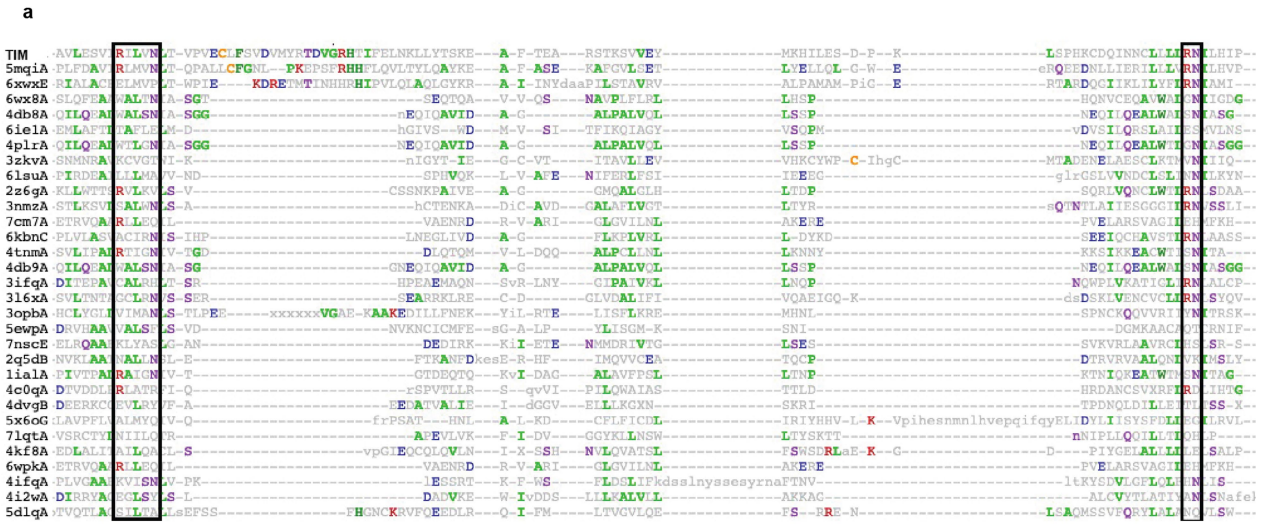

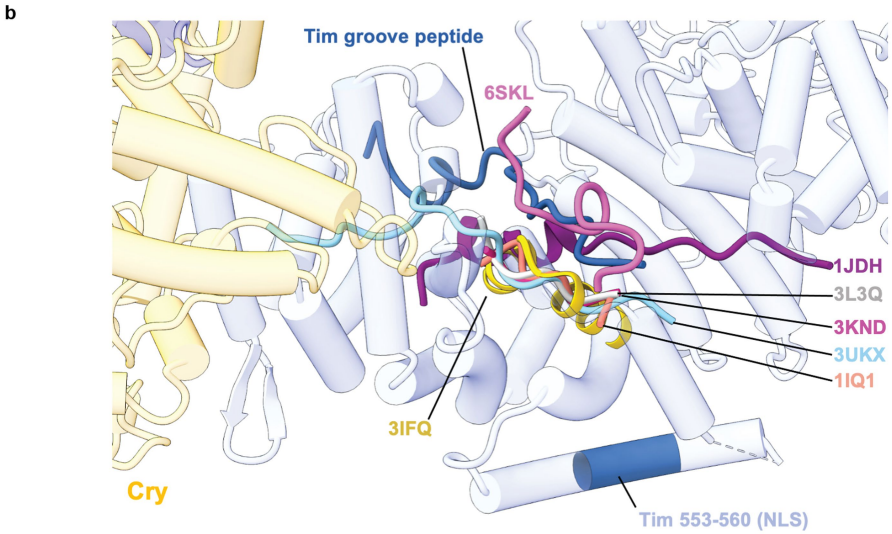

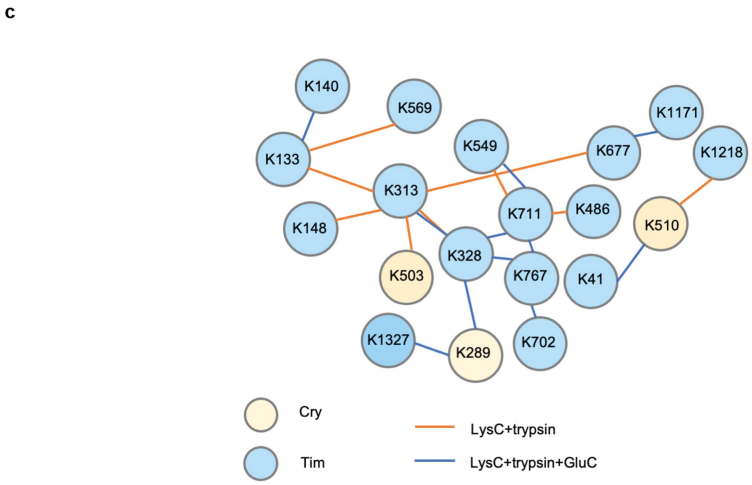

Extended Data Fig. 10 | See next page for caption.

Extended Data Fig. 10 | Interactions between Tim and its homologs with extended polypeptides in their respective ARM grooves in relation to crosslinking map of Cry-Tim. (a) Sequence alignment of top Tim structural homologs. Boxes outline the conserved R-XXX-N and RN residues within the ARM motifs that interact with the extended polypeptide chains of binding partners. Protein Data Bank (PDB) codes are shown on the left. (b) The extended peptide bound in the Tim groove resembles interactions found in other ARM-repeat proteins such as Importin-α1, β-catenin, and yeast TIM proteins. ARM-repeat proteins were structurally superimposed by their ARM-repeat cores to show the alignment of the extended peptides that bind in the crescent groove common to the family. For clarity only the groove peptides are displaced. Extended polypeptides found in yeast TOF1 (6SKL) and β-catenin (3IFQ) and Tim travel on the same lateral axis anti-parallel to the other importin-α, β-catenin, and Tim protein homologues. The PDB labels indicate the N terminus of the loop. 6SKL: Cryo-EM structure of the CMG Fork Protection Complex at a replication fork - Conformation 1 (lavender), 3IFQ: Interaction of plakoglobin and β-catenin with desmosomal cadherins (**gold**), 1JDH: Crystal structure of β-catenin and htcf-4 (**purple**), 3L3Q: Mouse importin α-pepTM NLS peptide complex (gray), 3KND: TPX2-importin-α complex (**magenta**), 1IQ1: Crystal structure of the importin-α(44–54)-importin-α(70–529) complex (**salmon**), 3UKX: Mouse importin-α:Bimax2 peptide complex (**sky blue**). (c) Map of DSSO lysine residue crosslinking defined by mass spectroscopy for the Cry-Tim complex. For the LysC+trypsin digested sample, although +2-charged peptides were excluded in the analysis, 59.79% sequence coverage for Cry and 49.81% for Tim were obtained. For the LysC+trypsin+GluC digested sample, 25.07% sequence coverage was obtained for Cry and 25.53% sequence coverage was obtained for Tim. Summary of the cross-links are given in the attached excel files and the raw data has been submitted to the PRIDE database.

nature portfolio

Corresponding author(s): Brian R. Crane

Last updated by author(s): Feb 1, 2023

Reporting Summary

Nature Portfolio wishes to improve the reproducibility of the work that we publish. This form provides structure for consistency and transparency in reporting. For further information on Nature Portfolio policies, see our Editorial Policies and the Editorial Policy Checklist.

Statistics

For all statistical analyses, confirm that the following items are present in the figure legend, table legend, main text, or Methods section.

n/a	Confirmed
☐	☒ The exact sample size (*n*) for each experimental group/condition, given as a discrete number and unit of measurement
☐	☒ A statement on whether measurements were taken from distinct samples or whether the same sample was measured repeatedly
☐	☒ The statistical test(s) used AND whether they are one- or two-sided *Only common tests should be described solely by name; describe more complex techniques in the Methods section.*
☒	☐ A description of all covariates tested
☒	☐ A description of any assumptions or corrections, such as tests of normality and adjustment for multiple comparisons
☐	☒ A full description of the statistical parameters including central tendency (e.g. means) or other basic estimates (e.g. regression coefficient) AND variation (e.g. standard deviation) or associated estimates of uncertainty (e.g. confidence intervals)
☐	☒ For null hypothesis testing, the test statistic (e.g. *F*, *t*, *r*) with confidence intervals, effect sizes, degrees of freedom and *P* value noted *Give P values as exact values whenever suitable.*
☒	☐ For Bayesian analysis, information on the choice of priors and Markov chain Monte Carlo settings
☒	☐ For hierarchical and complex designs, identification of the appropriate level for tests and full reporting of outcomes
☒	☐ Estimates of effect sizes (e.g. Cohen's *d*, Pearson's *r*), indicating how they were calculated

Our web collection on statistics for biologists contains articles on many of the points above.

Software and code

Policy information about availability of computer code

Data collection	EPU v2.10 (Thermo Fisher Scientific), for Cryo-EM data acquisition
Data analysis	MotionCor 2 (Zheng, S. Q. et al. MotionCor2: anisotropic correction of beam-induced motion for improved cryo-electron microscopy. Nat Methods 14, 331-332 (2017)), for movie alignment Relion v3.1.3 (Scheres, S. H. RELION: implementation of a Bayesian approach to cryo-EM structure determination. J Struct Biol 180, 519-530 (2012)), for Cryo-EM image processing CryoSparc v3.2.0 (Punjani, A., Rubinstein, J. L., Fleet, D. J. & Brubaker, M. A. cryoSPARC: algorithms for rapid unsupervised cryo-EM structure determination. Nat Methods 14, 290-296 (2017)), for Cryo-EM image processing Topaz v0.2.3 (Bepler, T. et al. Positive-unlabeled convolutional neural networks for particle picking in cryo-electron micrographs. Nat Methods 16, 1153-1160 (2019)), for particle picking UCSF ChimeraX v1.2.3 (Pettersen, E. F. et al. UCSF ChimeraX: Structure visualization for researchers, educators, and developers. Protein Sci 30, 70-82 (2021)), for structure visualization ISOLDE v1.0b3 (Croll, T. I. ISOLDE: a physically realistic environment for model building into low- resolution electron-density maps. Acta Crystallogr D Struct Biol 74, 519-530 (2018)), for initial model building SBGrid (Morin, A. et al. Collaboration gets the most out of software. Elife 2, e01456 (2013)), for integrating software

Phenix v1.20.1-4487 (Liebschner, D. et al. Macromolecular structure determination using X-rays, neutrons and electrons: recent developments in Phenix. Acta Crystallogr D Struct Biol 75, 861-877 (2019)), for model building

Coot v0.9.8 (Emsley, P., Lohkamp, B., Scott, W. G. & Cowtan, K. Features and development of Coot. Acta Crystallogr D Biol Crystallogr 66, 486-501 (2010)), for model building

MolProbity v4.2 (Chen, V. B. et al. MolProbity: all-atom structure validation for macromolecular crystallography. Acta Crystallogr D Biol Crystallogr 66, 12-21 (2010)), for modeling validation

Q-score v1.8.2 (Pintilie, G. et al. Measurement of atom resolvability in cryo-EM maps with Q-scores. Nat Methods 17, 328-334 (2020)), for modeling validation

RAPTORX v1.2.1 (Kallberg, M. et al. Template-based protein structure modeling using the RaptorX web server. Nature Protocols 7, 1511-1522 (2012)), for secondary structure prediction

Alphafold v2.2.4 as implemented in Colaboratory (Jumper, J. et al. Highly accurate protein structure prediction with AlphaFold. Nature 596, 583-589 (2021)), for de novo structure prediction
https://colab.research.google.com/github/deepmind/alphafold/blob/main/notebooks/AlphaFold.ipynb#scrollTo=wolxeCPygt7K

Xcalibur 4.3 (Thermo-Fisher Scientific) https://www.thermofisher.com/order/catalog/product/OPTON-30965

Proteome Discoverer (Thermo-Fisher Scientific)
https://assets.thermofisher.com/TFS-Assets/CMD/Application-Notes/AN-658-LC-MSn-PTM-Proteome-Discoverer-AN64831-EN.pdf

statistical significance (VassarStats; http://vassarstats.net). For Extended Figure 8, conditions were compared to WT dark by one-way ANOVA with a Tukey HSD post-hoc test for significance (Astatsa; https://astatsa.com)

For manuscripts utilizing custom algorithms or software that are central to the research but not yet described in published literature, software must be made available to editors and reviewers. We strongly encourage code deposition in a community repository (e.g. GitHub). See the Nature Portfolio guidelines for submitting code & software for further information.

Data

Policy information about availability of data

All manuscripts must include a data availability statement. This statement should provide the following information, where applicable:

- Accession codes, unique identifiers, or web links for publicly available datasets
- A description of any restrictions on data availability
- For clinical datasets or third party data, please ensure that the statement adheres to our policy

The cryo-EM density maps and the atomic model for TIM:CRY have been deposited in the EM Data Bank (EMDB: EMD-27335) and Protein Data Bank (PDB: 8DD7), respectively. The mass spectrometry proteomics data have been deposited to the ProteomeXchange Consortium via the PRIDE partner repository with the dataset identifier PXD034054. All other data such as protein gels for SWIFTI experiments are contained within the supplemental information. Reagents are available from the authors upon request.

Human research participants

Policy information about studies involving human research participants and Sex and Gender in Research.

Reporting on sex and gender	N/A
Population characteristics	N/A
Recruitment	N/A
Ethics oversight	N/A

Note that full information on the approval of the study protocol must also be provided in the manuscript.

Field-specific reporting

Please select the one below that is the best fit for your research. If you are not sure, read the appropriate sections before making your selection.

☒ Life sciences ☐ Behavioural & social sciences ☐ Ecological, evolutionary & environmental sciences

For a reference copy of the document with all sections, see nature.com/documents/nr-reporting-summary-flat.pdf

Life sciences study design

All studies must disclose on these points even when the disclosure is negative.

Sample size	For cryo-EM data, no statistical methods were used to estimate the initial sample size, i.e. the number of particles to be imaged; the sample size was increased until the final resolution and quality of the cryo-EM structures was no worse than 3.3 Å resolution as determined by gold-standard Fourier shell correlation (FSC) measurement. One biological sample contributed to the final structure as it provided the highest-resolution images and an electron density map that well-represented the amino-acid sequences and expected structures of the two proteins, although at least 3 individual biological replicates were imaged, all confirming the composition and overall structure of the complex to various resolutions.
Data exclusions	No data were excluded from the analysis. During cryo-EM data processing, images and particles were screened from the final reconstruction if they showed poor agreement or an inability to produce high-resolution features as determined by the accepted processing methods described in the paper and as reported in Table 1.
Replication	SWFTI analysis of CRY:TIM binding was performed on 3 biological replicates. Mass-spectrometry: Two different biological replicates of the CRY:TIM complex were cross-linked and analyzed by high-resolution mass-spectrometry. A GluC-LysC-Trypsin was used in one case and a LysC-Trypsin digest was used in the other, both produced cross-links consistent with the cryo-EM structure, as reported. There was no failure to replicate any experiments.
Randomization	Randomization of samples was not required because there was only one experimental group: the CRY:TIM complex. During image analysis, sets of single particle cryo-EM images were randomly assigned and compared for resolution determination by Fourier shell correlation; otherwise randomization was not relevant to this study.
Blinding	Blinding was not applicable to this study as there was no comparison groups.

Reporting for specific materials, systems and methods

We require information from authors about some types of materials, experimental systems and methods used in many studies. Here, indicate whether each material, system or method listed is relevant to your study. If you are not sure if a list item applies to your research, read the appropriate section before selecting a response.

Materials & experimental systems

n/a	Involved in the study
☐	☒ Antibodies
☐	☒ Eukaryotic cell lines
☒	☐ Palaeontology and archaeology
☒	☐ Animals and other organisms
☒	☐ Clinical data
☒	☐ Dual use research of concern

Methods

n/a	Involved in the study
☒	☐ ChIP-seq
☒	☐ Flow cytometry
☒	☐ MRI-based neuroimaging

Antibodies

Antibodies used	Supplier (NanoTagBiotechnologies), catalog name (ALFA Selector CE), CAT number (N1512), lot number (15200501). ALFA antibody was used as a 50% slurry in 4% cross-linked agarose per the manufactures protocol: https://nano-tag.com/technology/the-alfa-system/ Supplier (NanoTagBiotechnologies), catalog name (ALFA Peptide), CAT number (N1520-L), lot number (15220105). Nature Communications 2019; 10: 4403
Validation	Antibodies and target peptide were used for purification following the manufactures protocols and they performed as expected. No independent validation of the antibody was carried out; ALFA resin manufacturer statement: https://nano-tag.com/technology/the-alfa-system/; the construct containing the peptide tag was verified by DNA sequencing and the fused protein characterized by mass-spectrometry.

Eukaryotic cell lines

Policy information about cell lines and Sex and Gender in Research

Cell line source(s)	Drosophila S2 cell line (cat#CRL-1963) was purchased from ATCC (https://www.atcc.org/products/crl-1963).
Authentication	ATCC batch certified the cell line before shipping. Cell line was used for recombinant protein expression and performed as expected. Cell growth characteristics and visual health was monitored, which did not vary throughout the study. Proteins derived from the cell expression study were confirmed by peptide sequencing via mass-spectrometry, these included native cell proteins which were shown to have the amino acid sequences predicted by the cell genome.

Mycoplasma contamination	Cell lines were tested for mycoplasma contamination and showed none, nor any signs of health decline.
Commonly misidentified lines (See ICLAC register)	S2 cells are the only insect cell line that we work with in the laboratory, there was no opportunity for misidentification.